Effect of strain hardening on the rotation capacity of welded I-section high-strength steel beams

Wong, Wei Jun; Walters, Carey L.

Important note
To cite this publication, please use the final published version (if applicable).
Please check the document version above.

Effect of strain hardening on the rotation capacity of welded I-section high-strength steel beams

Wei Jun Wong & Carey L. Walters

Published online: 12 Apr 2023.

Submit your article to this journal ⬀

Article views: 244

View related articles ⬀

View Crossmark data ⬀

Taylor & Francis
Taylor & Francis Group

Effect of strain hardening on the rotation capacity of welded I-section high-strength steel beams

Wei Jun Wong and Carey L. Walters

Department of Maritime and Transport Technology, Delft University of Technology, Delft, The Netherlands

ABSTRACT

High-strength steel beams are known to have less plastic rotation capacity than beams with lower yield strengths. This has been related to the decreased strain-hardening ability of high-strength steels, and various rules and standards for steel structures stipulate maximum limits on the allowable yield-to-tensile strength ratio (σ_y/σ_u), which indirectly acts as a measure of strain hardening. While the literature suggests that there is an interdependence between strain hardening ability, yield strength, cross-sectional slenderness and rotation capacity, the presently prescribed limits on σ_y/σ_u (e.g. 0.91, 0.94, 0.95) are typically constant for a given material regardless of the other parameters mentioned. This computational study hence investigates how the rotation capacity is simultaneously dependent on yield strength, strain hardening ability and cross-sectional slenderness, and how each parameter affects the relationship between the others. The results show that, with the geometrical aspect kept constant through the use of normalised slenderness parameters, a higher yield strength leads to higher rotation capacity for a given σ_y/σ_u, while the well-known decrease of rotation capacity with higher σ_y/σ_u is confirmed. This suggests the possibility of more efficient use of high-strength steels with high σ_y/σ_u when the interdependence of all the variables are accounted for. The results also suggest the importance of accounting for the relative slendernesses of the web and the flange and whether the buckling behaviour is web- or flange-dominated, since a switch between a web- and flange- dominated buckling response could lead to a reverse in the trend between the rotation capacity and the overall cross-sectional slenderness.

Nomenclature

a	Weld throat size
B	Flange width
E	Young's modulus
e	Euler's number
G	Shear modulus
H	Beam depth
h	Web depth
I_w	Warping stiffness
I_z	Second moment of area about the minor axis
J	Torsion constant
K	Strength coefficient of the Hollomon power law
L	Modelled length of the beam
L_{in}	Length between the two loading points in 4-point-bending
L_{out}	Length between a support and the closest loading point
M	Moment of resistance
M_{cr}	Critical linear elastic buckling moment from linear bifurcation analysis
$M_{cr,LT}$	Critical linear elastic lateral-torsional buckling moment
M_{el}	Moment at first yielding
M_{pl}	Fully-plastic bending moment
n	Strain hardening exponent of the Hollomon power law
s	Weld leg length
t_f	Flange thickness
t_w	Web thickness
u	Magnitude of displacement
$u_{x,y,z}$	Displacement along x-, y- and z-axis respectively
ε	Yield stress scaling parameter
ε_y	Engineering yield strain
ε_t	True strain

θ	Cross-sectional rotation
$\theta_{4,end}$	4-point-bending end-rotation predicted by the pure-bending model
θ_{el}	Cross-sectional rotation corresponding to M_{el}
θ_{FE}	Total rotation from end-to-end of the pure-bending finite element model
θ_{pl}	Cross-sectional rotation corresponding to M_{pl} and assumed linear material behaviour
θ_{rot}	Cross-sectional rotation when M falls below M_{pl}
$\theta_{x,y,z}$	Rotation about x-, y- and z-axis respectively
κ	Curvature
κ_{pl}	Curvature corresponding to M_{pl} and assumed linear material behavior
λ_f	Flange slenderness
λ_{LT}	Lateral-torsional buckling slenderness
λ_p	Overall cross-section slenderness
λ_w	Web slenderness
σ_t	True stress
σ_u	Ultimate tensile stress
σ_y	Yield stress

1. Introduction

High-strength steels are increasingly used in the construction of ship and offshore structures due to their potential for reducing the weight and size of structural elements. However, such steels are known to have lower ductility, smaller reserve strength after yielding and reduced strain hardening ability relative to conventional lower-strength mild steels (Bannister and Trail 1996). They are also associated with a higher tendency to localise around stress concentrations (Obers et al. 2022). A description of the influence of

CONTACT Wei Jun Wong ✉ W.J.Wong@tudelft.nl 🖂 Department of Maritime and Transport Technology, Delft University of Technology, Mekelweg 2, Delft 2628 CD, The Netherlands

the hardening capacity (frequently indicated by the yield-to-tensile strength ratio σ_y/σ_u) on four failure modes can be found in Wong and Walters (2021). Risks of these failure modes remain a concern in the application of high-strength steels, and to account for this, various offshore, maritime and civil engineering rules, standards and specifications for steel structures stipulate requirements based on the σ_y/σ_u ratio (Appendix) and the fracture elongation. Specifically, European norms for the design of steel structures impose upper bounds of 0.91 (CEN 2005, 2020) and 0.95 (CEN 2007, 2020). A similar value of 0.94 is stipulated in the rules for the certification of high-strength shipbuilding and offshore steels by classification societies (DNV 2021b, 2021c; LR 2022b).

Given the aforementioned benefits of using high-strength steels, efforts have been made to find improved rules to account for ductility, so that higher-strength steels might be used with confidence. For example, recommendations on the acceptable σ_y/σ_u ratio in structures have been given based on considerations of the toughness, strength and deformation capacity of pressure vessels and pipelines (Bannister and Trail 1996), tubular joints (Billingham et al. 1997) and ties containing cross-sectional area reductions (Dhalla and Winter 1974; Sedlacek et al. 2008; Feldmann and Schaffrath 2017; Feldmann et al. 2020). However, the aforementioned limits of 0.91 (CEN 2005, 2020) and 0.95 (CEN 2007, 2020) correspond to recommendations which arise from the consideration of the rotation capacity at plastic hinges for steels with high σ_y and σ_y/σ_u ratios (Steenbergen et al. 1996; Feldmann and Schaffrath 2017; Pavlovic and Veljkovic 2017).

Although the dependence of the rotation capacity on σ_y/σ_u has been further evidenced by the work of several researchers on the topic (Kato 1990; Gioncu and Mazzolani 2002; Lee et al. 2013; Schillo and Feldmann 2017, 2018; Shi and Xu 2019), the relationship between σ_y/σ_u and the rotation capacity has yet to be quantified and explained definitively. The σ_y/σ_u limit of 0.91 prescribed in the latest draft of EN 1993-1-1 (CEN 2020) for the design by global plastic analysis agrees with Steenbergen et al.'s (1996) recommendation, which is derived from a cross-sectional treatment of classic beam mechanics and then-codified limits on the strain at uniform elongation (NEN 1990). However, this treatment neglected the role of plastic local buckling, which is a strong determinant of the ultimate failure behaviour of the hinge (Gioncu and Petcu 1997). Recent attempts have been made to determine the σ_y/σ_u limit appropriate for high-strength steel grades up to S960 based on experimentally-validated finite-element parametric studies considering buckling effects (Pavlovic and Veljkovic 2017), which resulted in recommendations for more stringent σ_y/σ_u limits by the authors, but these analyses were specific to hollow-section beams.

Furthermore, the context of the existing research (Ricles et al. 1998; Pavlovic and Veljkovic 2017) is a framework which makes use of broad, discrete cross-sectional classes to differentiate between levels of beam deformation capacity, such that the required σ_y/σ_u limit was investigated with particular focus on its relation to the separate flange and web slenderness ratios required to achieve a minimum rotation capacity. This separate classification of flange and web neglects the interactive effect between the constituent plates, and the approach of specifying a minimum rotation capacity corresponding to a broad, discrete definition of a ductility class is not conducive for describing the full continuous relationship between σ_y/σ_u and rotation capacities. Recent developments in the design of steel beam-columns have seen the use of a strain-based framework capable of estimating the strengths and deformation capacity of stocky cross-sections above the fully-plastic bending moment M_{pl} based on regression analysis of critical buckling strains dependent on

overall cross-sectional slenderness derived from finite element and experimental data (Gardner 2008; Lan et al. 2019), but these critical buckling strains themselves were not analysed for their dependence on the strain-hardening behaviour. To explore the limits of acceptable σ_y/σ_u ratios dependent on both the strain hardening and overall cross-sectional slenderness, this computational study investigates how the rotation capacity varies simultaneously with the yield strength σ_y, the σ_y/σ_u ratio which is used to characterise strain hardening (Section 3), and the overall cross-section slenderness λ_p, which accounts for relative web and flange slendernesses.

This study employs parametric finite element analyses of the bending of stocky I-section beams with varying material properties and geometries to describe the relationship between varying yield strengths, strain-hardening behaviours, and achievable rotation capacities in welded high-strength steel I-section beams. This structural form is chosen for its relevance considering the commonly applied method of analysing strips of plate-stiffener combinations in ship grillages as I-sections beams (Daley 2002; Hughes and Paik 2010) as well as its widespread use in civil engineering structures. The parametric investigation focuses on cross sections in the stocky range, i.e. cross sections with overall cross-sectional slenderness $\lambda_p < 0.51$ (Chen et al. 2022), because this is the range in which plasticity and strain hardening is expected to occur. Naturally, the dependence of the plastic local buckling behaviour on the web and flange slendernesses is also considered. Using the results of the parametric study, the σ_y/σ_u requirement of 0.94 by the classification societies (DNV 2021c; LR 2022b) is assessed together with the slenderness requirements of the IACS UR I Requirements concerning Polar Class (IACS 2019).

2. Rotation capacity and rotation requirements of plastic hinges

In the plastic design of structures, the ultimate strength of a structure is calculated based on the complete formation of a plastic collapse mechanism which results from a sequential formation of plastic hinges, so the rotation capacity R of a plastic hinge must be large enough so that the plastic hinge can maintain its strength until the complete collapse mechanism is formed. The rotation capacity R is defined as:

$$R = \frac{\theta_{rot}}{\theta_{pl}} - 1 \qquad (1)$$

where θ_{rot} is the rotation at which the moment resistance drops below the full-plastic bending moment M_{pl}, which is calculated based on a perfectly-plastic, fully yielded cross-section in bending, and θ_{pl} is the beam rotation corresponding to the M_{pl} based on ideal linearized behaviour (Figure 1).

The minimum required value for R depends on the structural and configuration, such as the number and length of the spans and the loading distribution on the different spans (Kuhlmann 1989). Although different values have also been suggested for specific cases (Korol and Hudoba 1972; Kemp 1984; Kuhlmann 1989), the general consensus in the literature is that an overall R requirement of 3 is sufficient for typical configurations encountered in building structures such as continuous beams and frames of typical proportions and loading (Yura et al. 1978; Stranghöner et al. 1994), and this was the value adopted for the structural steel code EN 1993-1-1 (Sedlacek and Feldmann 1995) and ANSI/AISC 360-16 (AISC 2016).
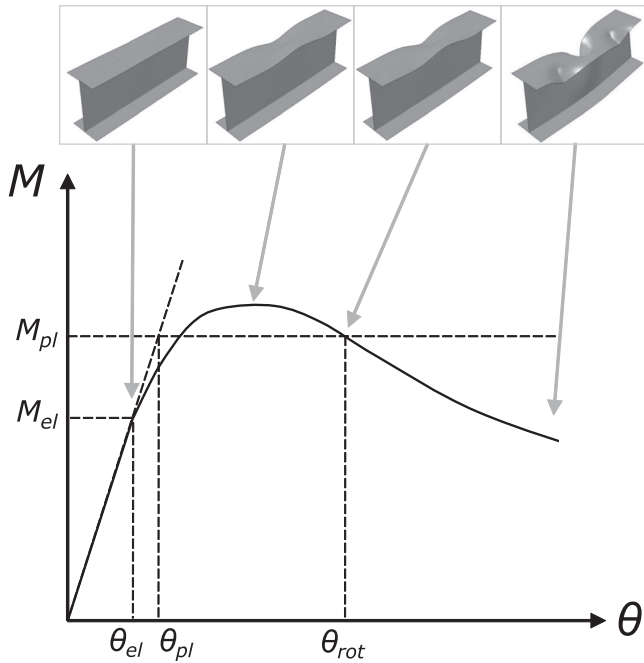
Figure 1. Rotation capacity (with deformation due to the application of uniform moment as example). (This figure is available in colour online.)

In the maritime industry, hull framings and grillages subject to lateral loading by ice (Daley 2002; IACS 2019), impacts (Zhu et al. 2018), and blasts (Yuan and Tan 2019) are also designed plastically and hence require sufficient structural ductility in the plastic range. In particular, plastic framing design concepts similar to that used in the civil structural industry are used for the design of hull grillages against ice loads (Daley 2002; IACS 2019). Similarly, limits are stipulated on the plate slenderness (IACS 2019) and the σ_y/σ_u ratio (DNV 2021c; LR 2022b). The authors are not aware of research on the rotation requirements specific to hull grillages. However, since the plate-stiffener combination in a hull grillage designed against lateral loading can be seen as a beam spanning over transverse girders (Hughes and Paik 2010), the rotation requirement of 3 applicable in general to multi-span continuous beam would be a reasonable value to adopt for the framing of hull grillages.

Accordingly, in assessing the current limits on σ_y/σ_u, λ_f, and λ_w in the classification society rules and UR I (IACS 2019), this paper adopts the minimum rotation requirement of 3. Nonetheless, the main focus of this paper is the slenderness- and strain-hardening-dependent rotation capacity rather than the rotation requirement, and the parametric studies shed light on the range of achievable rotation capacities and its influencing parameters regardless of rotation requirements.

3. The effect of the strain hardening ability on plastic local buckling and hinge rotation capacity

The primary failure mode that limits the strength and rotation capacity of plastic bending hinges is plastic local buckling that occurs after yielding develops over the cross section. Lateral-torsional buckling of the entire beam is excluded here, since the standard practice required by structural steel codes (CEN 2005; IACS 2019) is to eliminate lateral torsional buckling by either ensuring sufficient lateral restraint or limiting the unbraced length at the plastic hinges. In some situations, the rotation capacity could be limited by fracture on the tensile flange prior to local buckling due to stress concentrations due to the welding of web stiffeners; however, this should

be prevented in practice by appropriate welding and detailing practice (Lee et al. 2013). This paper hence focuses on the failure mechanism of plastic local buckling in unstiffened plastic hinges sufficiently designed against lateral torsional buckling.

Several attempts have been made to provide a physical explanation for the decreased rotation capacity of high strength steels which have high σ_y/σ_u ratios. Shi and Xu (2019) and Schillo and Feldmann (2017) related this to the absence of the yield plateau in the stress-strain behaviour of high-strength steels, which in conventional mild steels causes a 'jump' to larger strains and curvatures at the same level of loading. This can however only be a partial explanation, since it has been shown by Pavlovic and Veljkovic (2017) that even when comparing materials that all have rounded stress-strain curves, a higher σ_y/σ_u results in reduced rotation capacity. Steenbergen et al. (1996) related the reduction in the rotation capacity to the reduction in the plastic hinge length (the length over which yield has occurred) which accompanies higher σ_y/σ_u ratios, assuming first order beam kinematics and a specified failure strain criterion. This can once again only be a partial explanation, because it considers only pre-buckling behaviour, ignoring the crucial geometrically non-linear buckling mechanism which causes post-buckling drop-off in the moment resistance.

The most convincing proposition on what determines this behaviour is given by Kato (1965) and Schillo and Feldmann (2018), who identified the strain-hardening behaviour as an important factor in determining the rotation capacity of plastic hinges, although they neglected to quantify the relation between strain hardening and the rotation capacity. Nonetheless, Zhu and Leis (2005) showed that the σ_y/σ_u can be seen as a measure of the strain-hardening behaviour giving an overall measure of the slope and shape of the plastic stress-strain behaviour. By considering the uniaxial tensile test, assuming a Hollomon power curve (Equation (2)) which passes through the yield point for the plastic stress-strain behaviour, and applying Considère's 1885 necking instability criterion, they related the σ_y/σ_u ratio and the strain hardening exponent n of the Hollomon law, as shown in Equation (3). The significance of this is that the σ_y/σ_u ratio, despite being a ratio of two stresses and seemingly not related to strains, directly relates to the overall strain hardening behaviour of the assumed material law.

$$\sigma_t = K\varepsilon_t{}^n \qquad (2)$$

$$\frac{\sigma_y}{\sigma_u} = \frac{1}{1+\varepsilon_y}\left(\frac{e\ln(1+\varepsilon_y)}{n}\right)^n \qquad (3)$$

where σ_t is the true stress; ε_t is the true strain; K is the strength coefficient; and n is the strain hardening exponent ε_y is the engineering strain at yield; and e is Euler's number. Since high-strength steels are the focus on this research, a power-law true stress-strain curve acts as a reasonable and common choice (Bai and Wierzbicki 2010; Feldmann and Schaffrath 2017) for the true-stress strain curve.

In view of this, as few as two ubiquitously used parameters are sufficient to describe idealised true plastic stress-strain curves with a range of strain-hardening behaviour: the yield strength σ_y and the σ_y/σ_u ratio. The following analyses hence use the material definition as given by Equation (4) combined with Equation (3), which is fully defined given a combination of σ_y and σ_y/σ_u. This enables the use of σ_y/σ_u, in the computational study in this paper both as a strain hardening measure and as a direct variable input parameter whose effect on the model response behaviour is to be studied.

$$\sigma_t = \begin{cases} E\varepsilon_t & \text{for } \varepsilon_t \leq \varepsilon_y \\ K\varepsilon_t{}^n & \text{for } \varepsilon_t > \varepsilon_y \end{cases} \qquad (4)$$

4. Finite element model used for the parametric study

The welded I-section beam was modelled using 4-noded, reduced-integration, finite-strain shell elements (S4R) capable of capturing thick-shell behaviour and transverse shear deformation in Abaqus (DS Simulia 2019). The flanges were assigned with an appropriate offset in Abaqus so that the web was attached to the surface rather than the midsection of the flange shell elements in the finite element calculations.

To study the behaviour of the plastic hinge localisation independently from length-dependent moment gradient and global buckling effects, the beams in this study were loaded with a uniform moment along the length (pre-buckling) and modelled such that the non-dimensional lateral-torsional-buckling slenderness (Equation (5)) λ_{LT} was equal to 0.1. The parameter λ_{LT} is

$$\lambda_{LT} = \frac{M_{el}}{M_{cr,LT}} \tag{5}$$

where M_{el} is the moment at first yielding in the cross-section, and $M_{cr,LT}$ is the elastic critical buckling load, for which an exact solution exists for a beam loaded subject to a uniform moment, as is given by Equation (6) (Bažant and Cedolin 2010):

$$M_{cr,LT} = \frac{\pi}{L}\sqrt{EI_z GJ}\sqrt{1 + \frac{\pi^2}{L^2}\frac{EI_w}{GJ}} \tag{6}$$

where L is the length of the beam; E is the Young's modulus; I_z is the second moment of area about the minor axis; G is the shear modulus; I_w is the warping stiffness; and J is the torsion constant.

The value of λ_{LT} was arrived at by considering the threshold of $\lambda_{LT} < 0.4$ required to avoid lateral-torsional buckling (Trahair et al. 2008), the reduction of computational time achieved by analysing shorter beams, and the need to model a sufficient length such that the boundary conditions at the beam ends do not interfere with the buckling localisation in the plastic hinge. The constant λ_{LT} was achieved for different cross-sectional geometries by adjusting the length L of the model accordingly, which is found by substituting Equation (6) into (5) and solving for L.

To provide a uniform moment (pre-buckling), the beams were fully fixed at one end, and all the degrees of freedom of the nodes at the other end were kinematically coupled to a reference point on the same face, to which a rotation was applied to create major axis bending (Figure 2). The reference point was allowed to displace perpendicular to the major axis and longitudinally, but not in the direction perpendicular to the minor axis. Rotations of the reference point around the other two axes were also prevented.

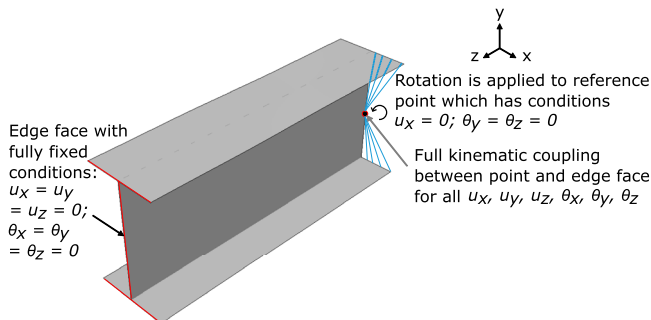The analyses are performed in displacement (rotation) control using Abaqus's general static solver, with automatic stabilisation to aid convergence in the unstable post-buckling range, as shown in Pavlovic and Veljkovic (2017). The dissipated energy fraction was specified as 0.0001, and the viscous damping energy was checked to be no more than 2% of the total internal energy. The through-thickness integration was performed using Simpson's rule with 25 through-thickness integration points, so that the post-buckling behaviour could be captured by the S4R elements even for the geometries with thicker walls, as shown by Sadowski and Rotter (2013).

4.1. Geometrical imperfections

Geometrical imperfections arising from the manufacturing and assembly of the welded I-section were accounted for in a conservative manner by applying an initial deformation in the shape of the elastic critical buckling mode obtained from a linear bifurcation analysis (LBA) performed using Abaqus. The buckling mode was given an amplitude equal to the assumed imperfection size, which was taken as 80% of the manufacturing tolerance, as recommended by EN 1993-1-5 (CEN 2006). The manufacturing tolerances of EN 1090-2 (CEN 2018) given for the flanges and webs of welded profiles were used, which are a $B/100$ out-of-squareness for the flange tip, and a $h/100$ out-of-plane deviation for the web, where B is the flange width and h is the depth of the web. When the peak of the buckled shape arose in the flange, the buckling mode was scaled by an imperfection size equal to $0.8B/100$, and when the peak of the buckled shape arose in the web, the buckling mode was scaled by an imperfection equal to $0.8h/100$.

4.2. Residual stresses from welding

The residual stress distribution (Figure 3) proposed by Schaper et al. (2022) for thermal-cut welded I-sections was introduced in the model. This distribution is based on studies on a range of steels including high strength steels up to grade S690 and accounts for the non-proportional relationship between the magnitude of the residual stresses and the yield strength. Furthermore, it accounts for the tensile stresses existing at the flange tips in thermal cut sections, which simultaneously causes higher compressive stresses in the flanges due to equilibrium conditions, affecting the buckling behaviour. In determining the size of the area (given by $\min\{t_w + 5a, B/5\}$) over the web-flange junction at which tensile residual stresses occur, the weld throat size a was taken to be $a = \sqrt{2}s/2 = 0.53t_w$, based on the typical conservative weld leg length of $s = 0.75t_w$ used for full-strength double-sided fillet welds (Blodgett 1963). However, the geometry of the weld was not included in the finite element model because it has a relatively small influence (Kucukler and Gardner 2021).

The residual stress distribution is nominally in equilibrium with itself. It was included in the model by introducing the predefined stress distribution throughout the beam (Figure 4) in the initial step of the analysis. This step is followed by a load-free static step to allow small stress imbalances caused by numerical inaccuracies and by the imposed geometrical imperfection to equilibrate, before any loading is applied.

4.3. Finite element model validation

The moment-rotation behaviour predicted by the finite element model is compared against that which is observed in experiments in the literature to validate the model's applicability. Four-point bending experiments on stocky high-strength welded I-section steel beams found in Green et al. (2002), Lee et al. (2013) and Yang et al. (2021) were considered. The experiments used for validation thus have high-strength steel grades (HSLA-80, HSA800 and
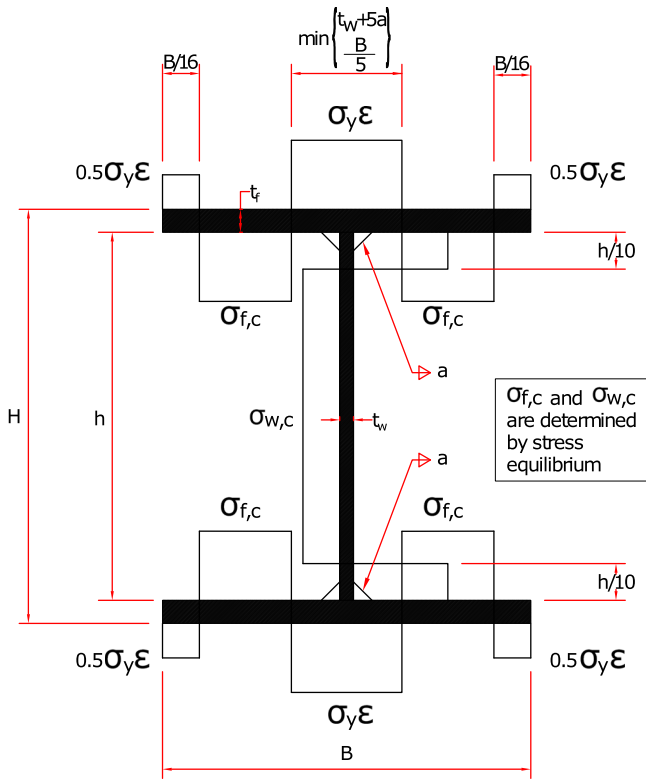
Figure 2. Boundary conditions and applied rotation. (This figure is available in colour online.)

Figure 3. Assumed residual stress distribution (Schaper et al. 2022). (This figure is available in colour online.)

Q690) and slendernesses ($\lambda_f < 10.1\varepsilon$; $\lambda_w < 72\varepsilon$ CEN 2005) which fall within the scope of the study.

The finite element model, which is subject to global bending through the application of an end rotation, is used to simulate the region between the two load application points in the four-point bending experiment, which likewise experiences a uniform moment over the length before buckling occurs. Appropriate
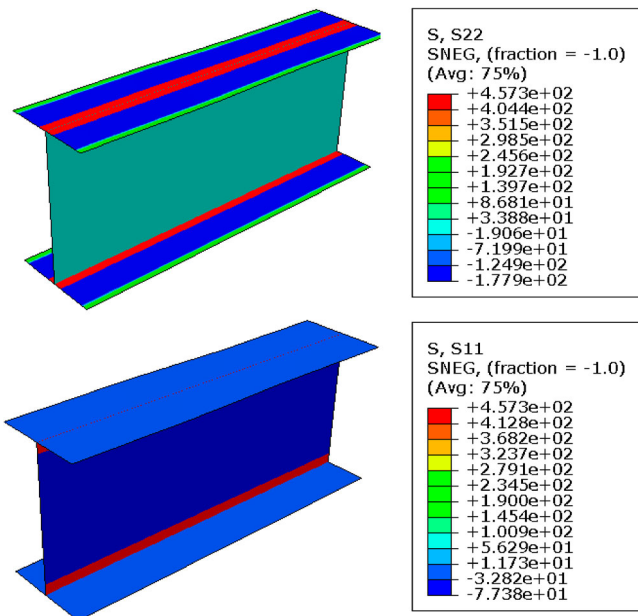
boundary conditions are added along the length of the finite element model to match lateral restraints applied in the experimental setup. A similar strategy has been successfully applied by Chen et al. (2022).

Since the experimental results were reported in terms of beam-end rotations of the 4-point bending setup while the finite element model only gives the rotations of the portion of the beam initially subjected to uniform moments, expected 4-point-bending beam-end rotations corresponding to the pure-bending model's end rotations were found using beam theory and the superimposition of the assumed-elastic response outside the pure bending region, as given by Equation (7).

$$\frac{\theta_{4,end}}{\theta_{pl}} = \frac{\theta_{FE} + \frac{L_{out}}{L_{in}}\min\left(\theta_{FE}, \theta_{pl}\right)}{L_{out}\kappa_{pl} + L_{in}\kappa_{pl}} \tag{7}$$

where $\theta_{4,end}$ is the 4-point-bending end-rotation predicted by the pure-bending model; θ_{FE} is the rotation at the rotated end of the pure bending model (while the other end is clamped in a horizontal position); L_{in} is the length between the two loading points; and L_{out} is the length between a support and the closest loading point. This results in predicted 4-point-bending beam-end rotations which are then plotted against the experimental 4-point-bending beam-end rotations.

To describe the material model in the finite element simulations, the engineering stress-strain curves reported by the authors of the experimental work were converted to true stress-strain values up to the ultimate tensile stress, followed by an extrapolation using the power curve as given in Section 3, with the exception of the experiment by Green et al. (2002) for which the full experimental stress-strain curve was not reported. In that case, Equations (2) to (4) were used to construct the true stress-strain curve, as described in Section 3.

Geometrical imperfections and residual stresses were included using the methods described above in Sections 4.1 and 4.2, while adopting the imperfection amplitude and yield stresses corresponding to the experiments, with the exception of the unreported imperfection amplitudes for the experiments by Lee et al. (2013) and Green et al. (2002). In those cases, estimates based on Eurocode recommendations (CEN 2006, 2018) as described in Section 4.1 were used.

The comparison in Figures 5–7 shows that the finite element models can simulate the moment-rotation behaviour observed in the experiments reasonably well.

Figure 4. Introduction of membrane residual stresses in flange (top) and in web (bottom) in Abaqus for $\sigma_y = 890$ MPa. (This figure is available in colour online.)
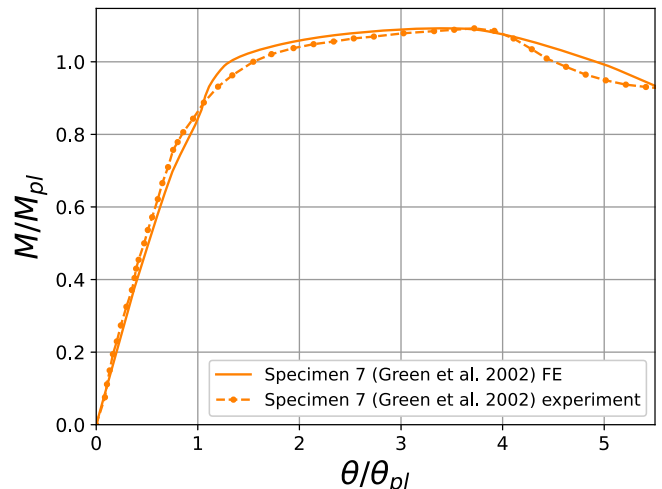

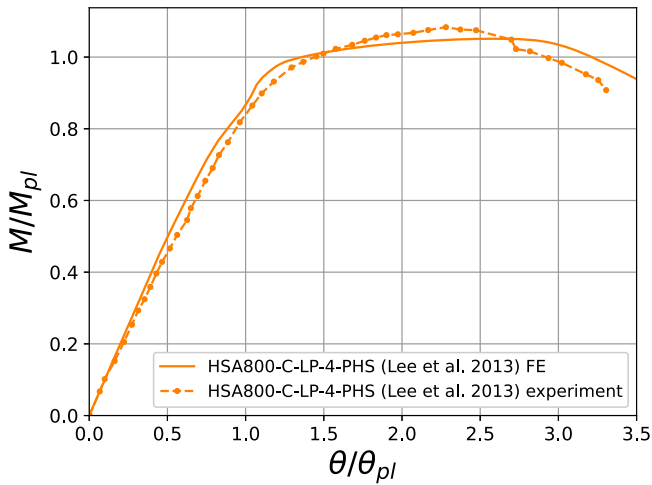**Figure 5.** Simulation of experiment from Green et al. (2002). (This figure is available in colour online.)

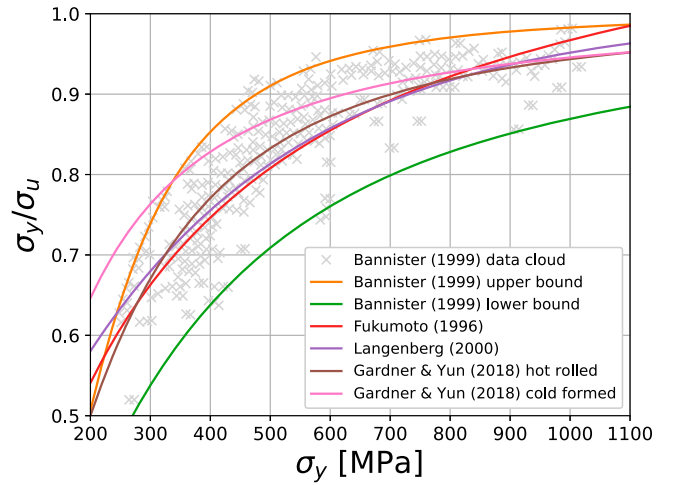**Figure 6.** Simulation of experiment from Lee et al. (2013). (This figure is available in colour online.)

Figure 8. Relationship between σ_y/σ_u and σ_y. (This figure is available in colour online.)

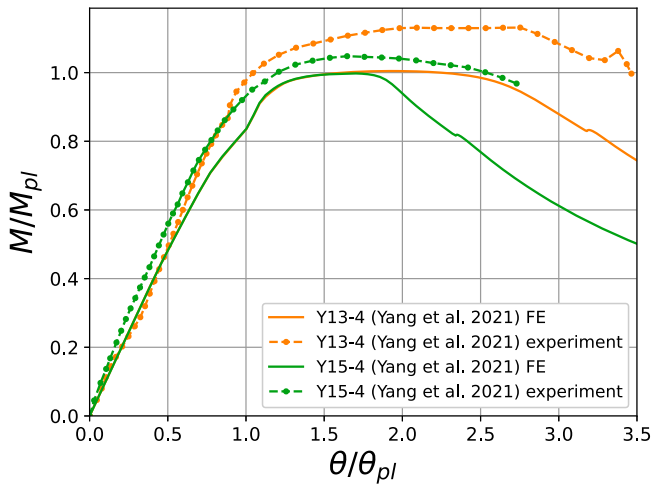**Figure 7.** Simulation of experiments from Yang et al. (2021). (This figure is available in colour online.)
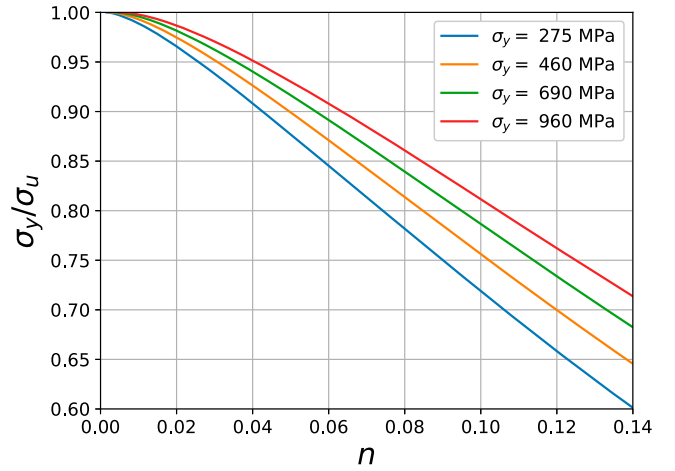

Figure 9. Plot of σ_y/σ_u against n (Equation (3)) for different σ_y. (This figure is available in colour online.)

It can be seen from Figures 5 and 6 that both the experimental curves by Green et al. (2002) and Lee et al. (2013) were captured very well in shape and reasonably well quantitatively. For Specimen 7 by Green et al. (2002), the model predicted the same maximum M/M_{pl} as observed in the experiment (within 0.02%) and overestimated the R by 11.9%. For test HSA800-C-LP-4-PHS by Lee et al. (2013), the model underestimated the maximum M/M_{pl} by 3.1% and overestimated the R by 15.3%.

The simulation of the experiments Y13-4 and Y15-4 (Figure 7) by Yang et al. (2021) also captured the maximum M/M_{pl} relatively well, overestimating it by 12.6% and 5.0% respectively. The prediction of the R showed greater deviations for these experiments, Y13-4 underestimating R by as much as 49.6% and Y15-4 not achieving any R at all. This is related to the definition of R, which being based on the exceedance of M_{pl}, is sensitive to changes in the maximum M/M_{pl} even if the post-buckling curve and decay do not change.

Table 1. Range of geometrical and material properties of the beams modelled in the parametric study.

Series	t_f [mm]	t_w [mm]	B [mm]	H [mm]	H/B	σ_y [MPa]	σ_y/σ_u	λ_f	λ_w	λ_p
1	20.0	17.6	200.0	400.0	2.0	[460, 960]	[0.80, 0.99]	[6.4ε, 9.2ε]	[28.6ε, 41.3ε]	[0.30, 0.42]
2	20.0	17.6	[153.0, 279.1]	450.8	[1.8, 2.9]	690	[0.80, 0.99]	[5.8ε, 11.2ε]	40.0ε	[0.30, 0.46]
3	20.0	17.6	[149.6, 247.8]	401.8	[1.8, 2.7]	890	[0.80, 0.99]	[6.4ε, 11.2ε]	40.0ε	[0.33, 0.45]
4	20.0	17.6	[217.5, 306.4]	[388.3, 543.2]	1.8	[460, 960]	[0.78, 0.99]	10.1ε	40.0ε	[0.38, 0.46]
5	15.0	11.0	220.0	400.0	1.8	[460, 960]	[0.80, 0.99]	[9.7ε, 14.1ε]	[47.1ε, 68.0ε]	[0.46, 0.65]
6	12.0	11.0	220.0	400.0	1.8	[460, 960]	[0.80, 0.99]	[12.2ε, 17.6ε]	[47.8ε, 69.1ε]	[0.54, 0.77]
7	12.0	11.0	152.5	[280.0, 480.0]	[1.8, 3.1]	690	[0.80, 0.99]	10.1ε	[39.9ε, 71.0ε]	[0.48, 0.56]
8	12.0	11.0	135.6	[250.1, 431.0]	[1.8, 3.2]	890	[0.80, 0.99]	10.1ε	[40.0ε, 72.0ε]	[0.52, 0.60]
9	12.0	11.0	[130.9, 184.3]	[309.7, 436.8]	2.4	[460, 960]	[0.78, 0.99]	10.1ε	52.5ε	[0.45, 0.56]

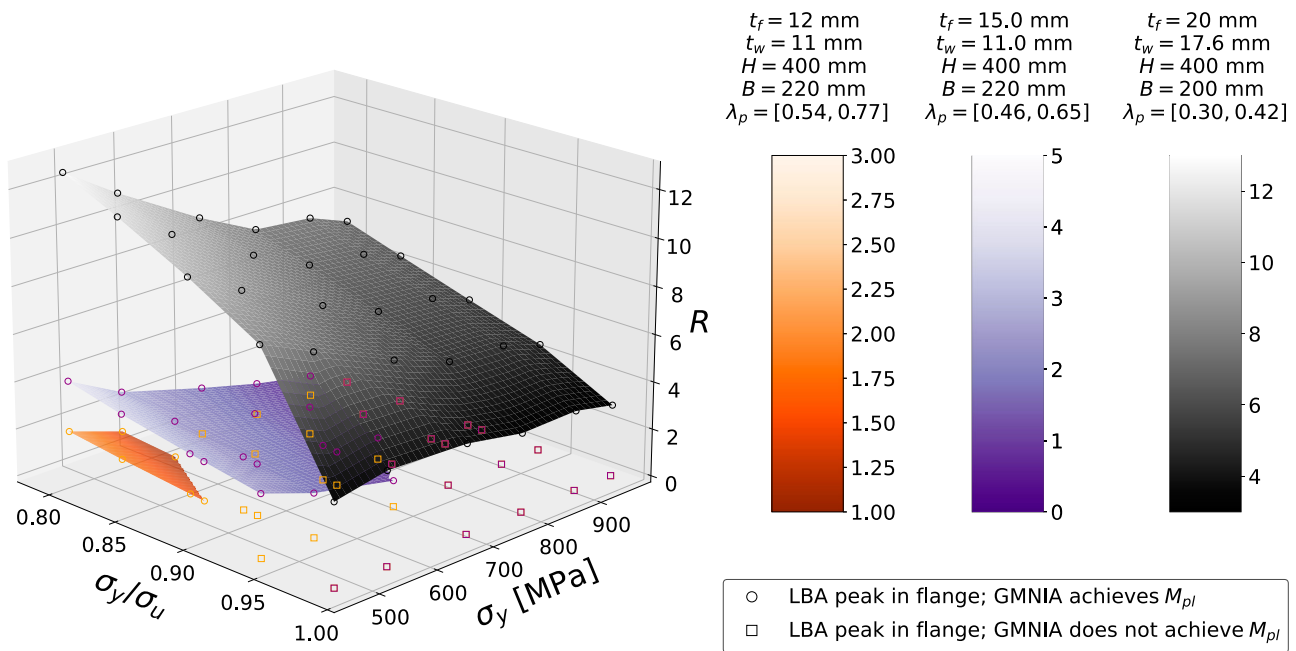**Figure 10.** R against σ_y/σ_u and σ_y. (This figure is available in colour online.)

However, these deviations in R were both underestimations by the model, acting on the conservative side. (Experiment Y11-4 by Yang et al. (2021) was not used for validation although it was stocky and tested in 4-point bending because it had a different lateral bracing system than all the other experiments modelled here and demonstrated very low R due to global buckling effects.)

The finite element modeling method has not been validated against other tests in Green et al. (2002), Lee et al. (2013) and Yang et al. (2021) because they either did not involve 4-point-bending setups or their slenderness fell out of the range of interest. It should hence be noted that the validation is limited to the scope described above, beyond which the results of this study should not be extrapolated.

5. Parametric studies

The finite element model was used to perform a series of imperfection-included geometrically and materially nonlinear analyses (GMNIA) of beams with varying geometries and material properties. 378 beams with varying yield strength σ_y, σ_y/σ_u ratio, width B, depth H, flange thickness t_f and web thickness t_w, were analysed, as summarised in Table 1. The model length L was correspondingly adjusted to maintain a constant lateral-torsional buckling slenderness λ_{LT}, as explained in Section 4.

5.1. Range of material properties in the parametric study

Figure 8 shows the relationship between σ_y and σ_y/σ_u as seen from existing tests from Bannister (1999), together with empirical relationships proposed by different researchers (Fukumoto 1996; Langenberg et al. 2000; Gardner and Yun 2018) based on other test databases. The experiments of Bannister (1999) involve steels
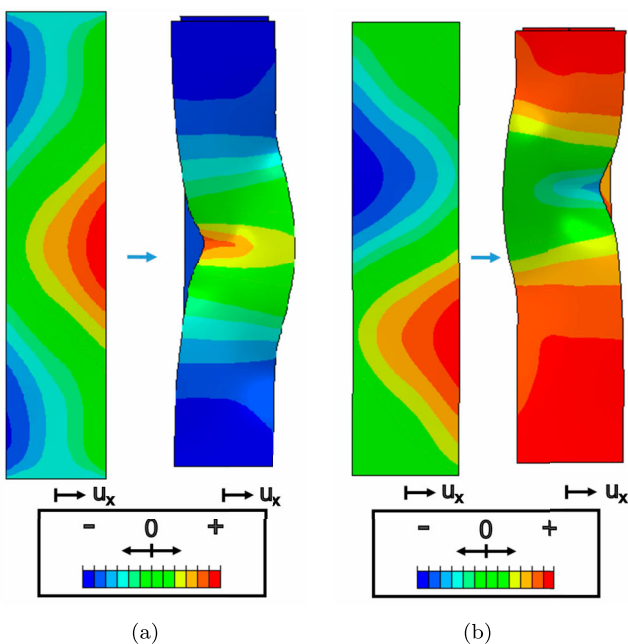

Figure 11. Buckling modes as seen from the top. (a) Symmetric buckling mode and (b) Asymmetric buckling mode. (This figure is available in colour online.)
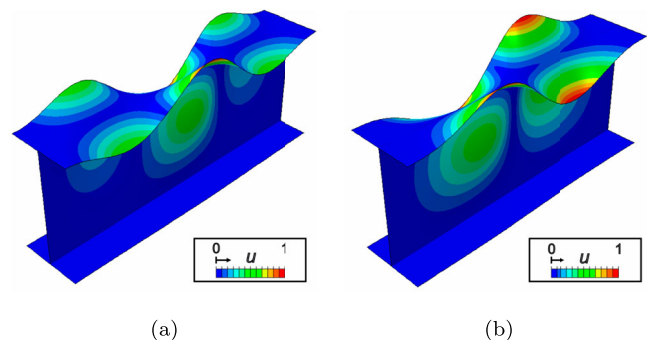

Figure 12. Linear elastic buckling mode shapes. (a) Odd number of LBA half wavelengths and (b) Even number of LBA half wavelengths. (This figure is available in colour online.)
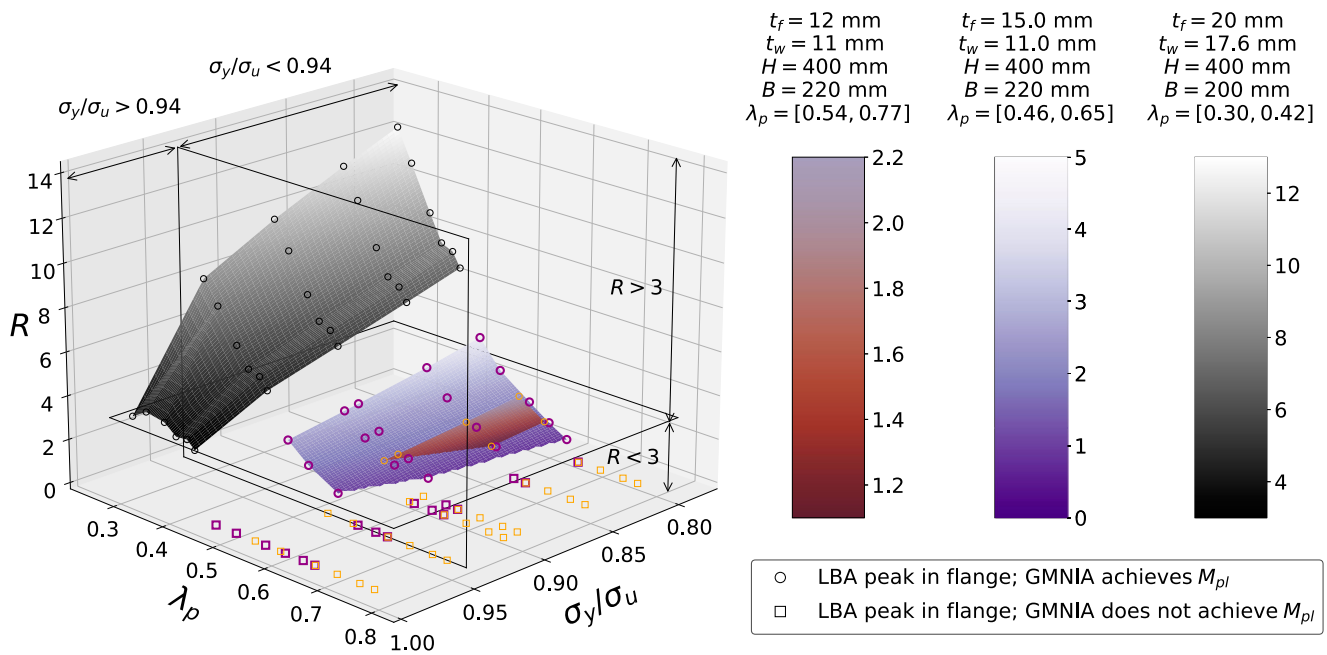
Figure 13. R against σ_y/σ_u and λ_p. (This figure is available in colour online.)

that are available for different industries, including the ship and offshore industry. Paik et al. (2017) tested several steels relevant to ships and offshore structures including steel grades A, D, AH32, DH32 and DH36, which would fall into the low-strength portion of this data cloud. The main focus of the current work concerns higher-strength steels, which are higher than most steels used in current practice in the maritime industry but well established in the offshore industry. These steels would fall into the higher strength region of the data cloud in Figure 8. This choice was made in order to focus on realistic steels with high σ_y/σ_u values.

The yield strength σ_y in the parametric study was hence varied assuming values of 460, 550, 690, 790, 890 and 960 MPa, and the σ_y/σ_u ratio was varied assuming values of 0.80, 0.84, 0.89, 0.94 and 0.99, with additional analysis points between these values when interpolating to make comparisons against the rules in UR I (IACS 2019). These ranges are common for high-strength steels, as seen in Figure 8. The generic stress-strain relationship that is given by the combination of Equations (3) and (4) and defined by the yield strength σ_y and the σ_y/σ_u ratio (which also directly acts as a strain hardening parameter) was utilised for this purpose.
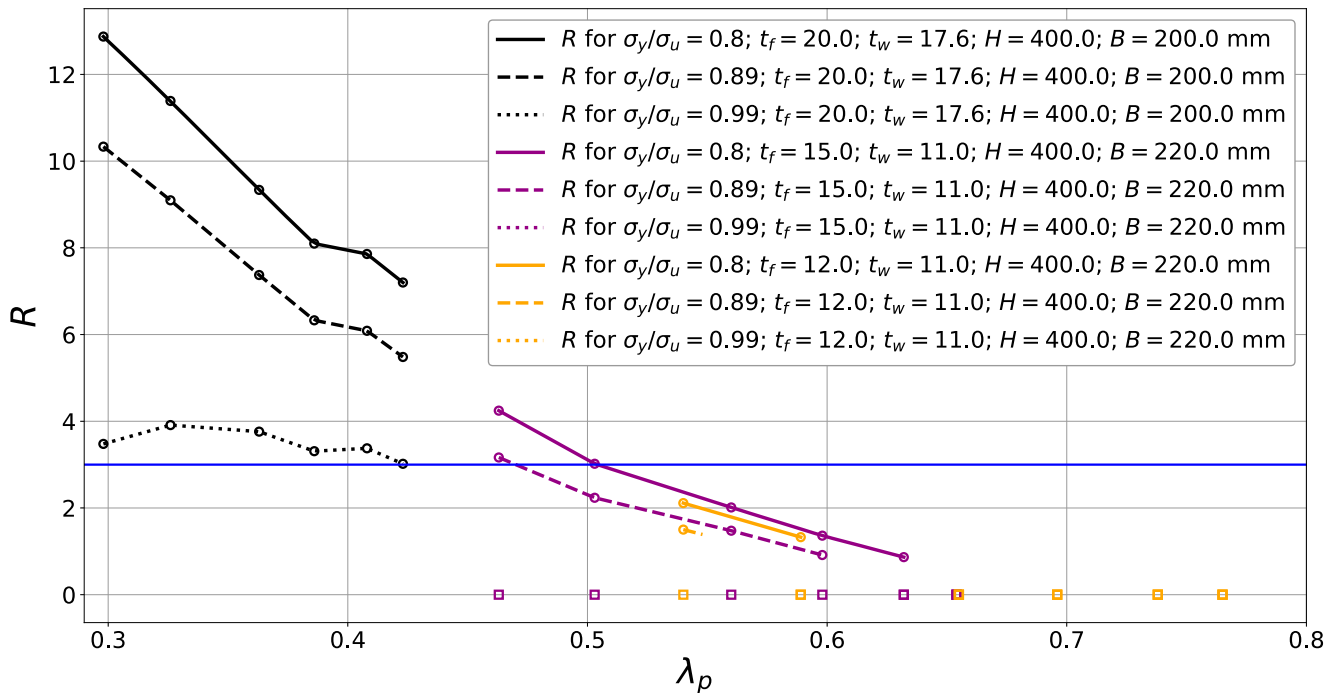

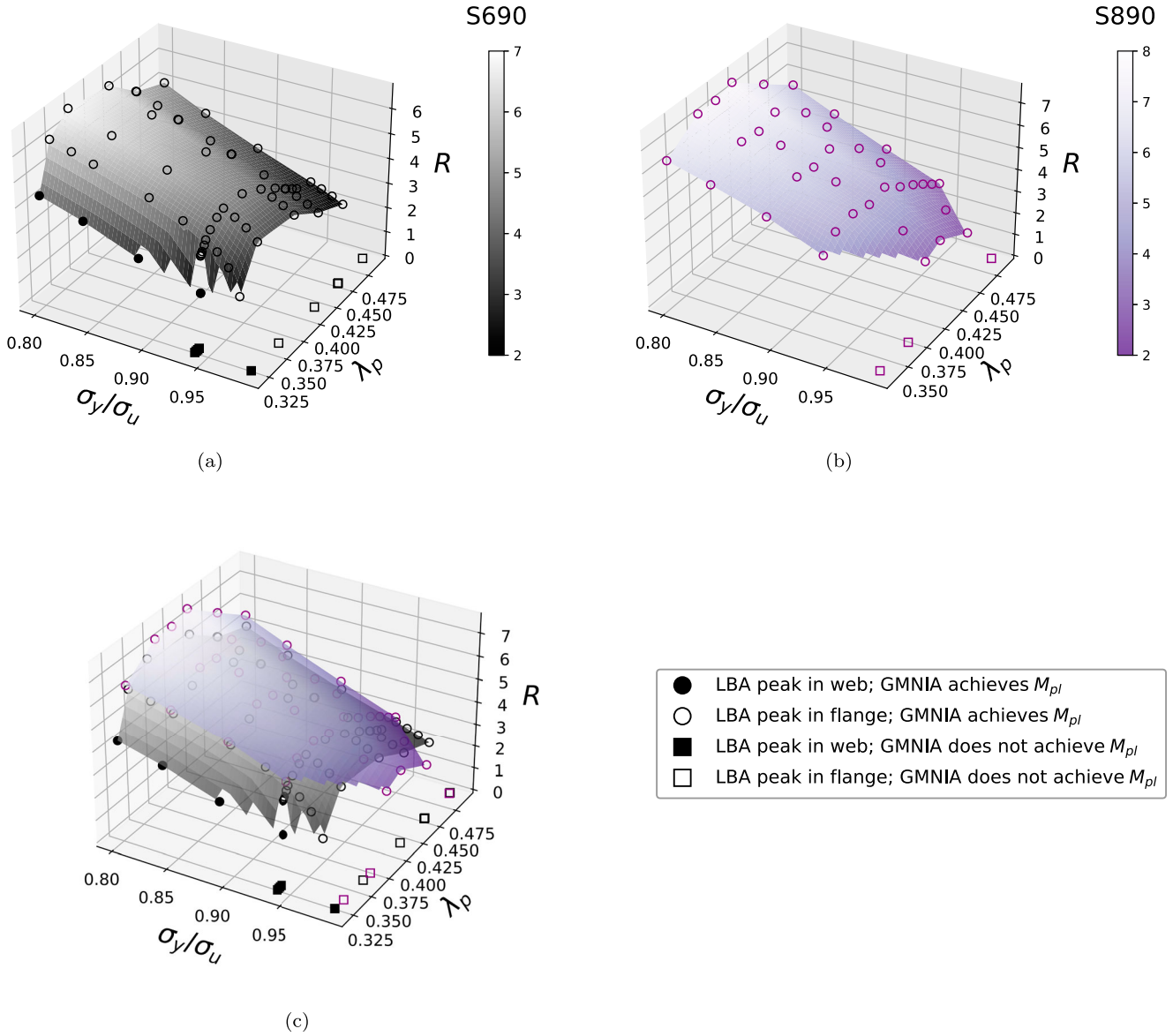**Figure 14.** R against λ_p for $\sigma_y/\sigma_u = 0.8$; 0.89 and 0.99. (This figure is available in colour online.)

Figure 15. R against σ_y/σ_u and λ_p for $t_f = 20.0$ mm; $t_w = 17.6$ mm; $\lambda_w = 40.0\varepsilon$. (a) $\sigma_y = 690$ MPa. (b) $\sigma_y = 890$ MPa and (c) $\sigma_y = 690$ MPa and $\sigma_y = 890$ MPa. (This figure is available in colour online.)

5.2. Range of geometrical properties in the parametric study

The ranges of the parameters B, H, t_f, t_w, were chosen such that the flange slenderness λ_f, web slenderness λ_w, overall cross-sectional slenderness λ_p, and depth-to-width ratio H/B fell near the limit and within the range for stocky I-sections with constituent plates which are also individually stocky. This corresponds to $\lambda_f < 10.1\varepsilon$ (IACS 2019), $\lambda_w < 72\varepsilon$ (CEN 2005, 2020) and $\lambda_p < 0.51$ (Chen et al. 2022). The yield stress scaling parameter ε and the slendernesses λ_f, λ_w, and λ_p are found as:

$$\varepsilon = \sqrt{\frac{235 \text{ MPa}}{\sigma_y}} \tag{8}$$

$$\lambda_f = \frac{B - t_w}{2t_f} \tag{9}$$

$$\lambda_w = \frac{h}{t_w} \tag{10}$$

$$\lambda_p = \sqrt{\frac{M_{el}}{M_{cr}}} \tag{11}$$

where M_{cr} is the elastic critical buckling moment of the overall cross-section, which is found by performing a linear bifurcation analysis of the beam subject to bending using Abaqus. Hence, for each set of parameters B, H, t_f, t_w, σ_y and σ_y/σ_u, a linear bifurcation analysis was first performed to obtain the buckling mode to be used as the shape of the geometrical imperfection and to obtain the critical buckling moment to be used to calculate λ_p. Then, a geometrically and materially non-linear static analysis with the assumed imperfections and residual stress distribution was performed using Abaqus to obtain the rotation capacity R as defined in Equation (1).

5.3. Dependence of rotation capacity on σ_y and σ_y/σ_u

Figure 8 shows a clear trend that steels with higher yield strengths σ_y typically have higher σ_y/σ_u ratios and that steels with the same σ_y could nonetheless have a significant variation in σ_y/σ_u. It is
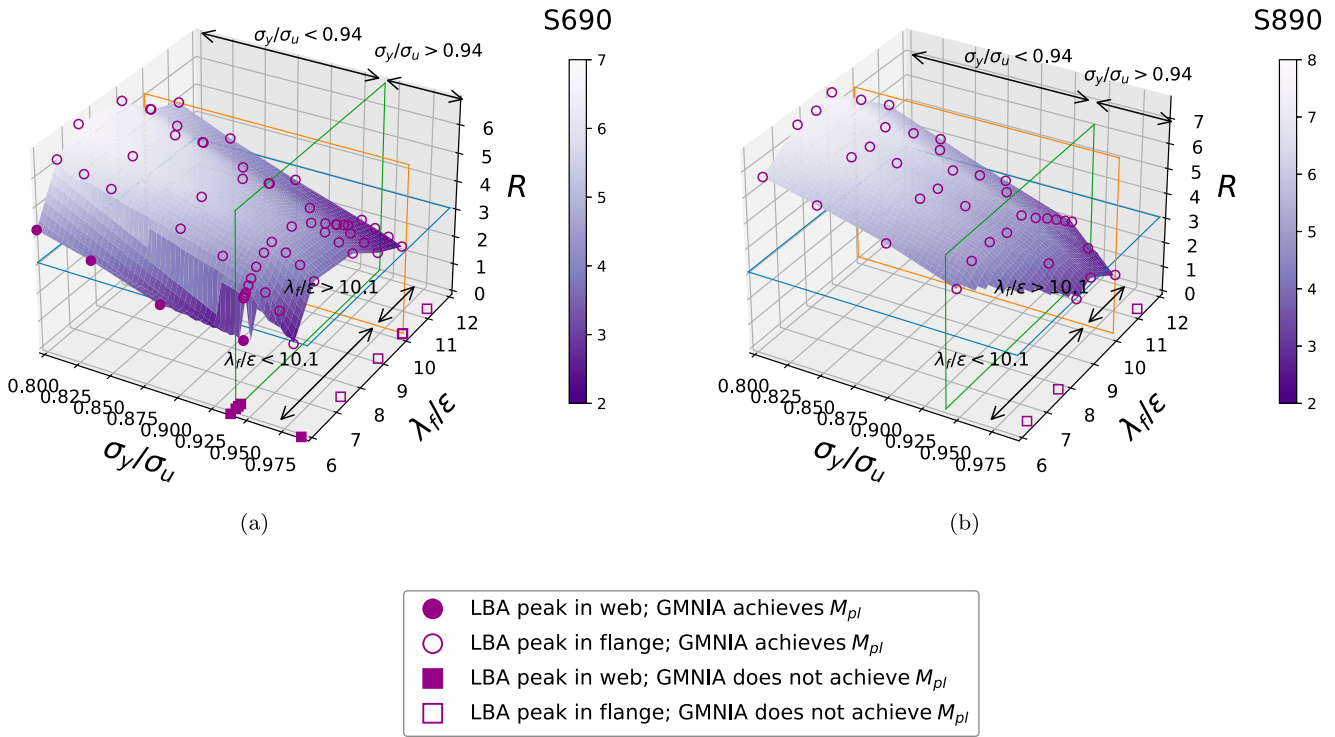
Figure 16. R against σ_y/σ_u and λ_f/ε for $t_f = 20.0$ mm; $t_w = 17.6$ mm; $\lambda_w = 40.0\varepsilon$. (a) $\sigma_y = 690$ MPa and (b) $\sigma_y = 890$ MPa. (This figure is available in colour online.)

Table 2. Expected σ_y/σ_u, λ_f and λ_w requirements for achieving $R = 3$ given existing classification limits.

	σ_y/σ_u	λ_f or λ_w	σ_y/σ_u	λ_f or λ_w
		690 MPa		890 MPa
Flange limit (for $t_f = 20.0$ mm; $t_w = 17.6$ mm; $\lambda_w = 40.0\varepsilon$)	**0.94**	**10.4ε**	**0.94**	**11.0ε**
	0.95	**10.1ε**	0.97	**10.1ε**
Web limit (for $t_f = 12.0$ mm; $t_w = 11.0$ mm; $\lambda_f = 10.1\varepsilon$)	**0.94**	42.1ε	**0.94**	43.9ε
	0.80	**52.5ε**	0.82	**52.5ε**

Values in bold font are the limits specified by the rules (DNV 2021c; LR 2022b); values in normal font are the inferred corresponding limits.

hence important to investigate the how R varies with σ_y and σ_y/σ_u simultaneously. It is also worth noting that the relationship between the σ_y/σ_u ratio and the strain hardening coefficient n given by Equation (3) is dependent on σ_y, as plotted in Figure 9. Steenbergen et al. (1996) presented results which showed that for a fixed σ_y/σ_u ratio, a higher σ_y leads to lower R, albeit without considering the occurrence of local buckling. The finite element analysis results plotted (Figure 10) and discussed below shows that the same trend is seen for failure by local plastic buckling at the plastic hinge.

In Figure 10, each colormap corresponds to a fixed cross-sectional geometry which has been analysed assuming a range of σ_y and σ_y/σ_u ratios. The effect of the different cross-sectional slendernesses is seen in the consistently higher R values achieved by the cross sections which are less slender. The analyses in which failure
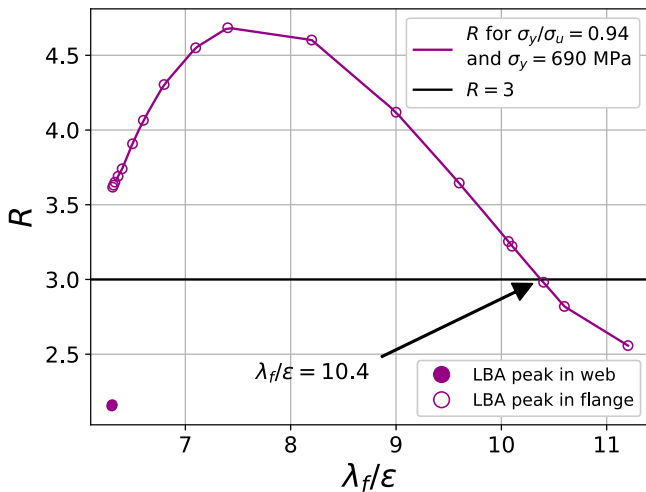

Figure 17. R against λ_f for $\sigma_y/\sigma_u = 0.94$ and $\sigma_y = 690$ MPa. (This figure is available in colour online.)
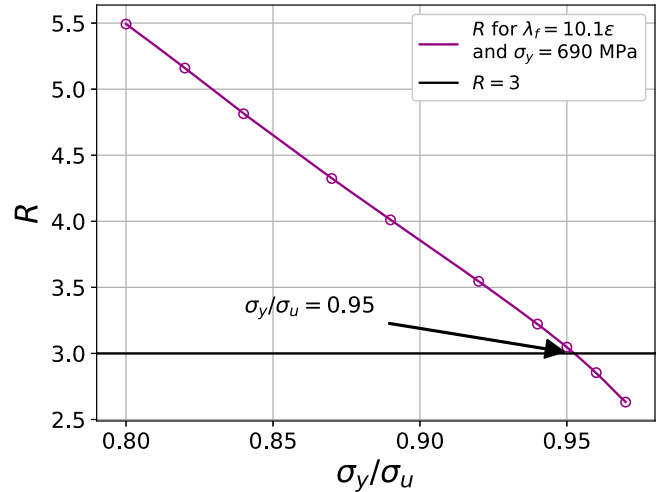

Figure 18. R against σ_y/σ_u for $\lambda_f = 10.1\varepsilon$ and $\sigma_y = 690$ MPa. (This figure is available in colour online.)
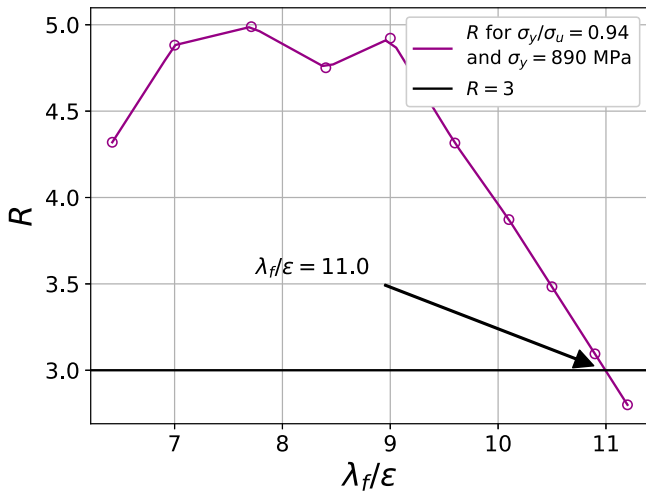
Figure 19. R against λ_f for $\sigma_y/\sigma_u = 0.94$ and $\sigma_y = 890$ MPa. (This figure is available in colour online.)

occurred before M_{pl} was reached are plotted on the figure as having R equal to 0. For the cross section with higher slenderness ($0.54 < \lambda_p < 0.77$), barely any of the analyses achieved the M_{pl}, let alone a R of 3. This agrees with Chen et al.'s (2022) classification that $\lambda_p < 0.51$ marks the range for which M_{pl} can be achieved.

Considering the cross section which falls in the stocky range indicated by the grayscale surface, the expected trend of decreasing R with increasing σ_y/σ_u is seen. As for the change in R given a fixed σ_y/σ_u and an increasing σ_y, a general decrease in R is seen, but with the presence of a small trough around $\sigma_y \approx 790$ MPa. Furthermore, the change in R with respect to σ_y becomes more gentle for higher σ_y/σ_u ratios. Looking into the buckled shapes of the finite element models, it can be seen that the trough around $\sigma_y \approx 790$ MPa is associated with a switching between a buckling mechanism which is symmetric, with a buckle localising in the center (such as in Figure 11(a)), and a buckling mechanism which is asymmetric, with a buckle localising in one half of the beam (such as in Figure 11(b)). Furthermore, the buckled plastic mechanism is related to the number of buckling half wavelengths present in the linear buckling mode shape: a symmetric mechanism is seen to happen when the LBA mode shape has an odd number of half wavelengths (Figure 12(a)), while an asymmetric mechanism is seen to happen
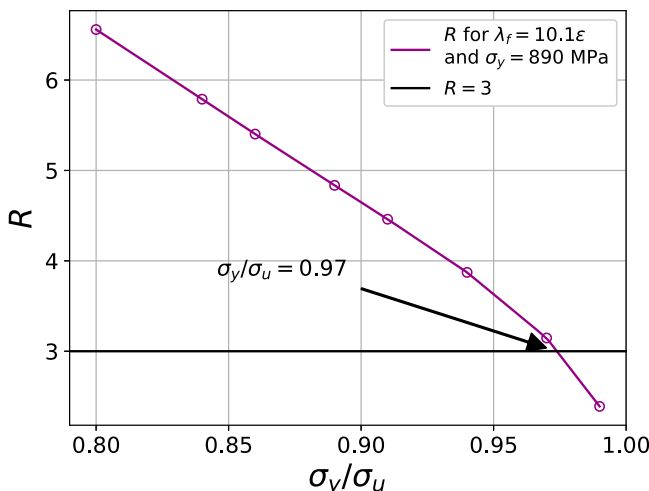
when the LBA mode shape has an even number of half wavelengths (Figure 12(b)).

This is even more clearly seen when R is plotted against λ_p in place of σ_y (Figure 13). Each plane of constant σ_y/σ_u gives a buckling curve showing the dependence of R on the slenderness λ_p (Figure 14), with mode switching causing small bumps in the curve. This is reminiscent of the plots of buckling strength against aspect ratio or dimensionless length used in linear elastic buckling analyses (Timoshenko and Gere 1961; Yamaki 1984), and speaks of the suitability of using λ_p as a normalised slenderness parameter in place of the traditional engineering use of λ_f, λ_w and $\varepsilon = \sqrt{235\,\text{MPa}/\sigma_y}$ separately. For a fixed cross-section geometry, the overall cross-section slenderness λ_p increases (linearly) if the σ_y increases, because λ_p is based on the normalisation of the critical elastic buckling load by σ_y (Equation (11)), and the critical elastic buckling load is independent of σ_y. Hence for a fixed cross-section geometry, increasing σ_y has an effect of increasing the normalised overall cross-section slenderness, which leads to a decreased R.

This buckling curve is however dependent on the σ_y/σ_u ratio. As can be seen in Figures 13 and 14, the overall height (in R) of each buckling curve decreases for higher σ_y/σ_u ratios. The switching between mode shapes is also different: around $\sigma_y \approx 550$ MPa ($\lambda_p \approx 0.33$) in the grayscale surface (representing stocky geometries), another switch into a different mechanism starts to occur for high σ_y/σ_u but not for lower σ_y/σ_u.

Therefore, the R does indeed decrease for increasing σ_y with increasing λ_p, and although the exact relationship is subject to the buckling mechanism and mode shape interactions, it has a decreasing trend overall. It will however be shown in the next section that an increasing σ_y paired with a constant λ_p leads instead to an increase in R.

5.4. Dependence of rotation capacity on σ_y/σ_u and λ_p

In Section 5.3, relationships between R, σ_y/σ_u, and σ_y (or λ_p as a linear function of σ_y) were plotted for fixed cross-sectional geometries. In this section, the effect of varying the σ_y/σ_u ratio and the cross-sectional geometry for a fixed σ_y is investigated instead. The flange thickness t_f and the web thickness t_w are fixed at 20.0 mm and 17.6 mm respectively. The λ_p is varied by changing the flange slenderness while keeping the web slenderness λ_w fixed at 40.0ε, which corresponds to $H = 450.8$ mm for $\sigma_y = 690$ MPa and $H = 401.8$ mm for $\sigma_y = 890$ MPa.

In this case, the solution of Equations (5) and (6) to maintain a constant $\lambda_{LT} = 0.1$ works out such that the analyses for a fixed σ_y have roughly the same length, i.e. between 1152.1 mm and 1152.3 mm for $\sigma_y = 690$ MPa and between 898.8 mm and 898.9 mm for $\sigma_y = 890$ MPa.

Figure 15(a) shows the resulting R-σ_y/σ_u-λ_p relationship for $\sigma_y = 690$ MPa. As before, an increase in σ_y/σ_u leads to a decrease in R for a given λ_p. A small trough is seen in the R surface with respect to λ_p at around $\lambda_p \approx 0.45$, corresponding to a switch between a symmetrical and asymmetrical buckling mode as also seen in Section 5.3 above. Nonetheless, there is a maximum point in the variation of R with respect to λ_p at $\lambda_p \approx 0.36$ despite there being no change in the overall buckling mode there. This can be related to the decreasing ratio of the maximum flange displacement to the maximum web displacement in the LBA mode shape with decreasing λ_f and λ_p, which culminates in a transition of the location of the peak displacement in the mode shape from being in the flange to being in the web. The latter leads to what is here termed 'web-dominated' buckling behaviour and the former to 'flange-dominated' buckling behaviour. The unexpected trend of a decreasing R with increasing stockiness (i.e. decreasing λ_p) when the imperfection peak is in the web rather
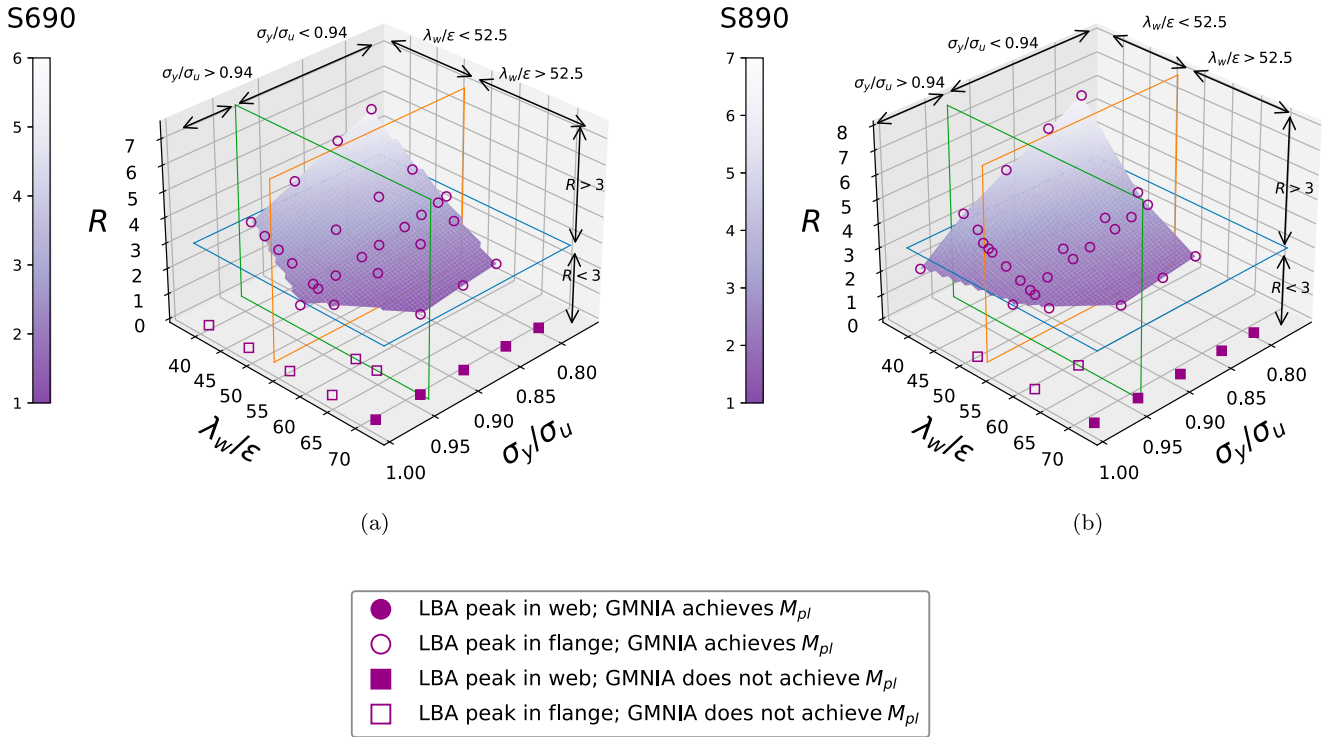

Figure 20. R against σ_y/σ_u for $\lambda_f = 10.1\varepsilon$ and $\sigma_y = 890$ MPa. (This figure is available in colour online.)

Figure 21. R against σ_y/σ_u and λ_w/ε for $t_f = 12.0$ mm; $t_w = 11.0$ mm; $\lambda_f = 10.1\varepsilon$. (a) $\sigma_y = 690$ MPa and (b) $\sigma_y = 890$ MPa. (This figure is available in colour online.)

than the flange demonstrates that web-dominated buckling behaviour and large web imperfections could be more detrimental to R than flange-dominated buckling behaviour, and it is necessary to consider both situations.

It is important to note that all of the analyses here have the same $\lambda_w = 40.0\varepsilon$, which satisfies the maximum web slenderness limit specified in UR I (IACS 2019) to prevent local web buckling and also satisfies the EN 1993-1-1 (CEN 2005, 2020) Class 1 limit for web plates. The switch in the mode shape's peak location led to a change in trend and a decrease in R despite a decrease in λ_f and λ_p and a constant λ_w classified as sufficiently stocky. It is hence important to either account for the location of the buckling mode or imperfection peak or consider limits on the relative ratio between flange and web slenderness.
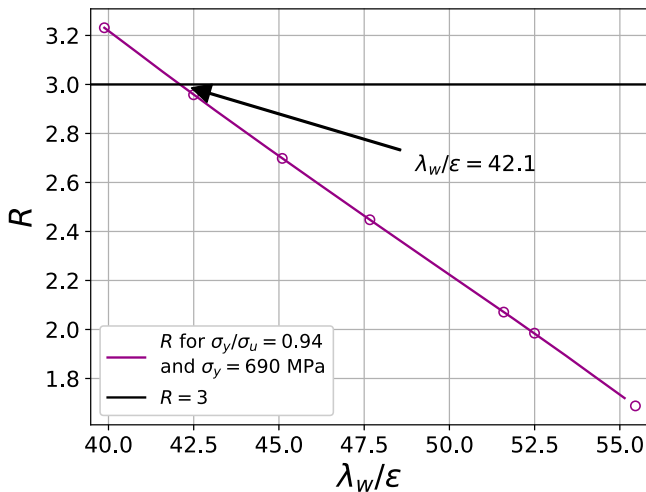
For $\sigma_y = 890$ MPa (Figure 15(b)), a similar overall trend to that of $\sigma_y = 690$ MPa discussed above is seen, where for a constant σ_y/σ_u, the gradient of R with respect to λ_p is positive for small λ_p and negative for large λ_p, and a small trough is seen at around $\lambda_p \approx 0.39$ which is associated with a switching from an asymmetrical buckling mode to a symmetrical buckling mode as discussed in Section 5.3 above.

Figure 15(c) shows the R-σ_y/σ_u-λ_p relationship assuming the same fixed t_f and t_w, for both $\sigma_y = 690$ MPa and $\sigma_y = 890$ MPa. While for a fixed cross-section geometry, an increase in σ_y leads to an increase in λ_p such that R decreases (Figure 13), Figure 15(c) shows that for a fixed λ_p, an increase in σ_y leads to an increase in R. This is in agreement with the idea a higher strain hardenability leads to greater R, because if the normalised slendernesses λ_{LT} and λ_p are fixed (by accordingly adjusting the cross-section geometry), any increase in σ_y is a purely material change, and for a fixed σ_y/σ_u ratio, a higher σ_y leads to a greater n and a greater strain hardening ability, since the behaviour of σ_y/σ_u as a strain hardening parameter is dependent on σ_y (Equation (3) and Figure 9).

6. Assessment of the UR I flange and web slenderness limits

As discussed in Section 2, grillages subject to ice loading in polar class ships are designed using plastic framing design concepts in which the plate-stiffener combination is assumed to act as a frame which develops plastic hinges (Daley 2002; IACS 2019). UR I (IACS 2019) specifies a maximum flange-outstand slenderness limit of $155/\sqrt{\sigma_y} = 10.1\varepsilon$ and a web slenderness limit of $282/\sqrt{\sigma_y} = 52.5\varepsilon$ (where the yield stress is in MPa) to prevent local flange and web buckling in the welded stiffeners. As an example to illustrate the significance of the trends observed from the parametric study, the aforementioned slenderness limits are assessed together with the σ_y/σ_u limit of 0.94 specified in the classification societies' rules (DNV 2021c; LR 2022b) for two
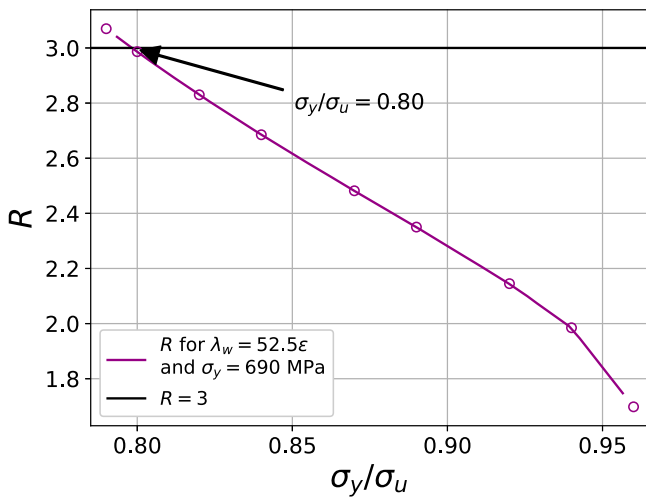

Figure 22. R against λ_w for $\sigma_y/\sigma_u = 0.94$ and $\sigma_y = 690$ MPa. (This figure is available in colour online.)

Figure 23. R against σ_y/σ_u for $\lambda_w = 52.5\varepsilon$ and $\sigma_y = 690$ MPa. (This figure is available in colour online.)

nominal steel grades, $\sigma_y = 690$ MPa and $\sigma_y = 890$ MPa. Since R is dependent on both the cross-sectional slenderness and σ_y/σ_u, the slenderness required to achieve a given R depends on the σ_y/σ_u ratio, and the σ_y/σ_u ratio required to achieve a given R depends on the slenderness. The results of the parametric study is hence used to infer a limiting slenderness corresponding to the σ_y/σ_u limit of 0.94 in the classifications societies' rules (DNV 2021c; LR 2022b) and similarly a limiting σ_y/σ_u ratio corresponding to the slenderness limits in UR I, based on the assumptions described in Sections 4 and 5. As shown in Figures 16 to 25, this is done by using linear interpolation of the parametric results and plotting lines describing a constant σ_y/σ_u, λ_f/ε or λ_w/ε.

The same series of parametric analyses discussed in Section 5.4 is considered to assess the λ_f limit, since this series has a constant and stocky web slenderness and varying flange slendernesses. As for assessing the λ_w limit, a series of finite element analyses with a fixed stocky web slenderness λ_w of 10.1ε is performed. The flange and web thicknesses are fixed at $t_f = 12.0$ mm and $t_w = 11.0$ mm, and λ_{LT} is set to 0.1 as before. The values obtained are summarised in Table 2.

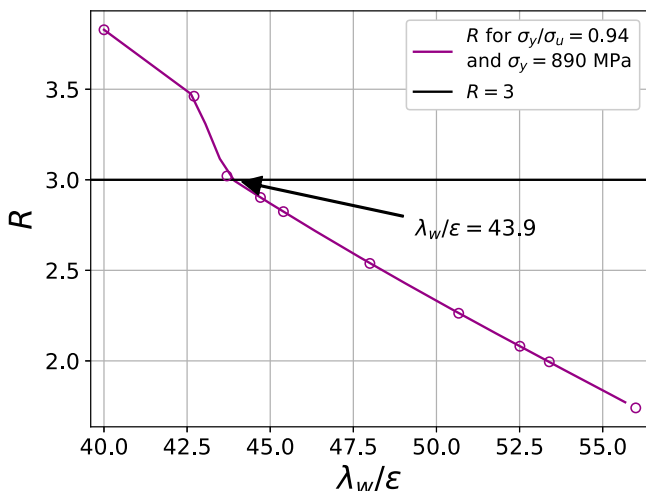For the given $\sigma_y/\sigma_u = 0.94$ limit, the 890 MPa steel could achieve an R of 3 with a higher plate slenderness (λ_f/ε or λ_w/ε)

than could the 690 MPa steel. For a fixed plate slenderness, the maximum σ_y/σ_u to achieve an R of 3 is higher for the 890 MPa steel than for the 690 MPa steel. This is in line with the observation in Section 5.4 that a higher yield strength leads to a higher R when the σ_y/σ_u and the normalised slendernesses are fixed. Considering the trend that higher strength steels tend to have higher σ_y/σ_u ratios, stipulating requirements on σ_y/σ_u, λ_f/ε and λ_w/ε which are dependent on σ_y or appropriately normalised to σ_y has the potential for allowing more efficient use of high-strength steels.

The results here suggest that for higher strength steels such as the 690 MPa and 890 MPa steel considered in this example, the limits on σ_y/σ_u relating to λ_f/ε are sufficient for achieving the $R = 3$ threshold, but the σ_y/σ_u and λ_w/ε limits are not. However, it should be noted that the interdependence between λ_w/ε and λ_f/ε has not been studied in these sections, since the λ_f/ε limit was investigated for a fixed λ_w/ε, and vice versa. Further studies either considering a combined overall cross-section slenderness or explicit considering λ_w/ε-λ_f/ε interdependence are required. Designs could also be optimised by investigating more precise R requirements the framing in grillage systems.

In Figures 17 and 19, the transition at low λ_f/ε into web-dominated buckling behaviour (with the LBA peak occurring in the web as discussed in Section 5.4) becomes relevant as R threatens to decrease below 3 even while the slenderness is decreasing. Figure 17 even sees a sudden drop below $R = 3$ once the gradual transition of the location of the LBA peak displacement to the web is complete. It is hence recommended that web- and flange- dominated buckling are both considered or that a limit on the ratio between web and flange slenderness is included to avoid loss of rotation capacity despite low web and flange slendernesses.

By varying the σ_y and σ_y/σ_u for beams with constant t_f, t_w, λ_f, λ_w and λ_{LT}, the σ_y/σ_u requirement with respect to σ_y for beams with constant cross-sectional slenderness classifications can be assessed. This is done by plotting the R-σ_y-σ_y/σ_u data and using linear interpolation to find the σ_y-σ_y/σ_u line corresponding to $R = 3$. To illustrate this, two series of parametric runs involving constant cross-sectional slendernesses were performed: one with $t_f = 20.0$ mm; $t_w = 17.6$ mm; $\lambda_w = 40.0\varepsilon$ and $\lambda_f = 10.1\varepsilon$ (Table 1, Series 4); and another with $t_f = 12.0$ mm; $t_w = 11.0$ mm; $\lambda_w = 52.5\varepsilon$ and $\lambda_f = 10.1\varepsilon$ (Table 1, Series 9). The results are plotted in Figure 26, together with the empirically derived trends between σ_y and σ_y/σ_u observed in steels (from Figure 8). Thus, in Figure 26, the solid lines can be seen as the upper bound of

Figure 24. R against λ_w for $\sigma_y/\sigma_u = 0.94$ and $\sigma_y = 890$ MPa. (This figure is available in colour online.)
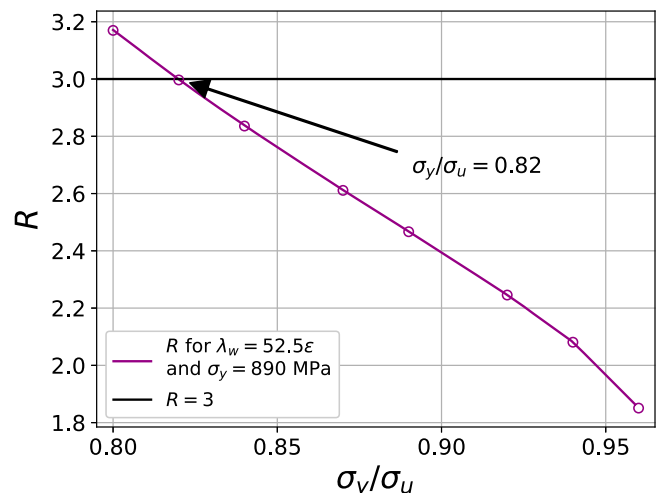

Figure 25. R against σ_y/σ_u for $\lambda_w = 52.5\varepsilon$ and $\sigma_y = 890$ MPa. (This figure is available in colour online.)
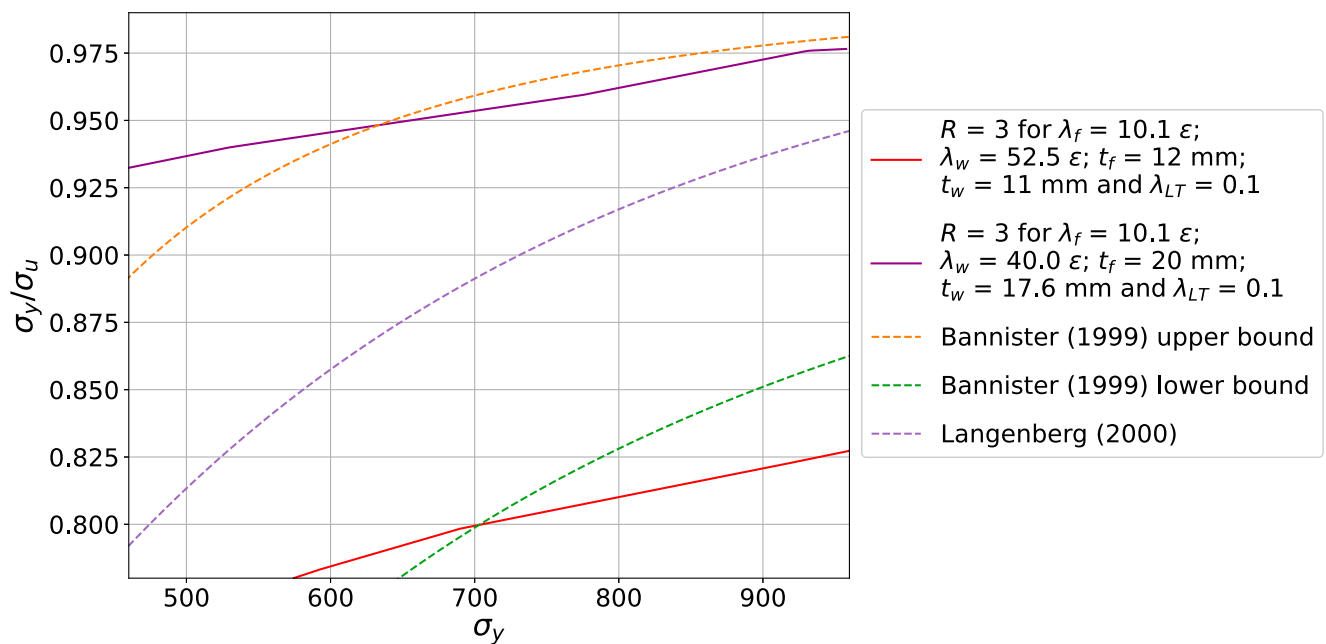
Figure 26. Observed and required σ_y/σ_u against σ_y based on geometry from Series 4 and 9 (Table 1). (This figure is available in colour online.)

what is acceptable for the given geometry based on considerations of the plastic rotation capacity, while the dashed lines can be seen as describing the range over which high-strength steel properties are found. It shows that for rotation capacity considerations, the local slenderness of the structure plays a big role on whether or not the σ_y/σ_u is adequate. Furthermore, it shows that while the observed values of σ_y/σ_u generally increases with σ_y, the highest tolerable σ_y/σ_u ratio required to achieve sufficient rotation capacity also increases, reiterating the relevance of ductility and slenderness requirements that are simultaneously dependent on σ_y and σ_y/σ_u.

7. Conclusions

This study has shown that the rotation capacity R is simultaneously dependent on the yield strength σ_y, the σ_y/σ_u ratio and the cross-section slenderness (λ_f, λ_w or λ_p). The following conclusions may be drawn from this study:

(1) Due to the interdependence between R, σ_y, σ_y/σ_u and λ, a complete, accurate determination of the σ_y/σ_u limit would, in the ideal case, be situational and dependent on the desired rotation and specific geometries, in contrast to the current practice which typically involves a material-specific limit that is independent of the structure.
(2) For a fixed σ_y/σ_u ratio, cross-sectional slenderness and lateral-torsional buckling slenderness, a higher σ_y leads to higher rotation capacities. This suggests that increased use of high-strength steels could be achieved by considering all of these factors together. For example, this could be done by introducing cross-sectional slenderness limits that are dependent on both the σ_y and σ_y/σ_u, instead of a constant, blanket σ_y/σ_u requirement such as is currently adopted in standards and rules.
(3) The trend between the rotation capacity and the cross-sectional slenderness depends on the relative slendernesses of the web and the flange and whether the buckling is web- or flange-dominated. Increasing the flange stockiness by decreasing the flange width for a beam that is experiencing web-dominated buckling does not help to increase the rotation capacities but

instead decreases it, although a decrease is reflected in the cross-section slenderness parameter. This suggests the importance of considering the relative slendernesses of the web and the flange, in contrast to the current practice in UR I (IACS 2019), EN 1993-1-5 (CEN 2005) and ANSI/AISC 360-16 (AISC 2016) and of specifying independent web and flange limits, as also suggested by Chen et al. (2022).

ORCID

Wei Jun Wong 🅓 http://orcid.org/0000-0002-2818-9533

References

AISC (American Institute of Steel Construction). 2016. ANSI/AISC 360-16 specification for structural steel buildings.
API (American Petroleum Institute). 2018. API 5L. Line pipe specification 5L.
ASTM (American Society for Testing and Materials). 2019. A913/913M-19 standard specification for high-strength low-alloy steel shapes of structural quality, produced by Quenching and self-tempering process.
ASTM (American Society for Testing and Materials). 2020. A992/A992M-20 Standard specification for structural steel shapes.
Bai Y, Wierzbicki T. 2010. Application of extended mohr–coulomb criterion to ductile fracture. Int J Fract. 161:1–20.
Bannister AC. 1999. SINTAP report – Structural integrity assessment procedures – Sub-task 2.3: yield stress/tensile stress ratio: results of experimental programme (SINTAP/BS/25). Report. British Steel PLC.
Bannister AC, Trail SJ. 1996. SINTAP report – Structural integrity assessment procedures – Sub-task 2.1: The significance of the yield stress/tensile stress ratio to structural integrity. Report. British Steel PLC.

Bažant ZP, Cedolin L. 2010. Stability of structures. Singapore: World Scientific Publishing Co. Pte. Ltd. DOI:10.1142/7828.

Billingham J, Healy J, Bolt H. 1997. The significance of yield ratio and work-hardening for structural performance. marine research review 9. Report. Marine Technology Directorate.

Blodgett OW. 1963. Design of weldments. Cleveland (OH): The James F. Lincoln Arc Welding Foundation.

BV (Bureau Veritas). 2020. NR 216 Amd 002 Rules on materials and welding for the classification of marine units.

CEN (European Committee for Standardization). 2005. EN 1993-1-1 Eurocode 3: design of steel structures – Part 1–1: general rules and rules for buildings.

CEN (European Committee for Standardization). 2006. EN 1993-1-5 Eurocode 3: design of steel structures – Part 1–5: plated structural elements.

CEN (European Committee for Standardization). 2007. Eurocode 3: design of steel structures – Part 1–12: additional rules for the extension of EN 1993 up to steel grades S700.

CEN (European Committee for Standardization). 2018. EN 1090-2 Execution of steel structures and aluminium structures – Part 2: technical requirements for steel structures.

CEN (European Committee for Standardization). 2019. EN 10225 Weldable structural steels for fixed offshore structures – Technical delivery conditions.

CEN (European Committee for Standardization). 2020. prEN 1993-1-1 Draft: eurocode 3: design of steel structures – part 1–1: general rules and rules for buildings.

Chen S, Fang H, Liu Jz, Chan TM. 2022. Design for local buckling behaviour of welded high strength steel I-sections under bending. Thin Wall Struct. 172: Article ID 108792.

Considère A. 1885. Mémoire sur l'emploi du fer et de l'acier. Ann Ponts Chaussées. 9:574–775.

Daley CG. 2002. Derivation of plastic framing requirements for polar ships. Mar Struct. 15:543–559.

Dhalla AK, Winter G. 1974. Suggested steel ductility requirements. J Struct Div. 100:445–462.

DNV (Det Norske Veritas). 2021a. DNV-ST-F101 Submarine pipeline systems.

DNV (Det Norske Veritas). 2021b. DNVGL-OS-B101 Offshore standard: metallic materials.

DNV (Det Norske Veritas). 2021c. Rules for classification: ships: part 2 materials and welding.

DS Simulia (Dassault Systémes Simulia). 2019. ABAQUS 2019.HF2. Commercial Finite Element Software.

Feldmann M, Schaffrath S. 2017. Assessing the net section resistance and ductility requirements of en 1993-1-1 and en 1993-1-12. Steel Constr.

Feldmann M, Schaffrath S, Sandro C. 2020. Draft: Background document to eurocode 3 en 1993 – part 1-10: Material toughness – approach for upper-shelf toughness requirements for the design of steel structures based on damage mechanics. Report.

Fukumoto Y. 1996. New constructional steels and structural stability. Eng Struct. 18:786–791.

Gardner L. 2008. The continuous strength method. Proc Inst Civil Eng Struct Build. 161(SB3):127–133.

Gardner L, Yun X. 2018. Description of stress-strain curves for cold-formed steels. Constr Build Mater. 189:527–538.

Gioncu V, Mazzolani F. 2002. Ductility of seismic resistant steel structures. London: Spon Press.

Gioncu V, Petcu D. 1997. Available rotation capacity of wide-flange beams and beam-columns part 2. experimental and numerical tests. J Constr Steel Res. 43:219–244.

Green PS, Sause R, Ricles JM. 2002. Strength and ductility of hps flexural members. J Constr Steel Res. 58:907–941.

Hughes OF, Paik JK. 2010. Ship structural analysis and design. New Jersey: The Society of Naval Architects and Marine Engineers.

IACS (International Association of Classification Societies). 2019. IACS UR I Requirements concerning polar class.

ISO (International Organization for Standardization). 2019. ISO 3183 Petroleum and natural gas industries – Steel pipe for pipeline transportation systems.

Kato B. 1965. Buckling strength of plates in the plastic range. Vol. 25. Zürich: Verlag Leemann. p. 127–141. DOI:10.5169/seals-20352

Kato B. 1990. Deformation capacity of steel structures. J Constr Steel Res. 17:33–94.

Kemp AR. 1984. Slenderness limits normal to the plane of bending for beam-columns in plastic design. J Constr Steel Res. 4:135–150.

Korol RM, Hudoba J. 1972. Plastic behavior of hollow structural sections. J Struct Div. 98:1007–1023.

Kucukler M, Gardner L. 2021. In-plane structural response and design of duplex and ferritic stainless steel welded I-section beam–columns. Eng Struct. 247:113136.

Kuhlmann U. 1989. Definition of flange slenderness limits on the basis of rotation capacity values. J Construct Steel Res. 14:21–40.

Lan X, Chen J, Chan TM, Young B. 2019. The continuous strength method for the design of high strength steel tubular sections in bending. J Constr Steel Res. 160:499–509.

Langenberg P, Nießen T, Dahl W. 2000. Bruch- und verformungsverhalten von hochfesten stählen mit streckgrenzen von 690 bis 890 MPa. Stahlbau. 69:283–291.

Lee CH, Han KH, Uang CM, Kim DK, Park CH, Kim JH. 2013. Flexural strength and rotation capacity of I-shaped beams fabricated from 800 MPa steel. J Struct Eng. 139:1043–1058.

LR (Lloyd's Register). 2022a. Code for lifting appliances in a marine environment.

LR (Lloyd's Register). 2022b. Rules for the manufacture, testing and certification of materials.

NEN (Nederlands Normalisatie-Instituut). 1990. NEN 6770 TGB 1990 – Staalconstructies – Basiseisen en basisrekenregels voor overwegend statisch belaste constructies.

Obers SFPM, Overal JJ, Wong WJ, Walters CL. 2022. The effect of the yield to tensile strength ratio on stress/strain concentrations around holes in high-strength steels. Mar Struct. 84:Article ID 103205.

Paik JK, Kim KJ, Lee JH, Jung BG, Kim SJ. 2017. Test database of the mechanical properties of mild, high-tensile and stainless steel and aluminium alloy associated with cold temperatures and strain rates. Sh Offshore Struct. 12: S230–S256.

Pavlovic M, Veljkovic M. 2017. Compact cross-sections of mild and high-strength steel hollow-section beams. Proc Inst Civil Eng. 170(SB11):825–840.

Ricles JM, Sause R, Green PS. 1998. High-strength steel: implications of material and geometric characteristics on inelastic flexural behavior. Eng Struct. 20:323–335.

Sadowski AJ, Rotter JM. 2013. Solid or shell finite elements to model thick cylindrical tubes and shells under global bending. Int J Mech Sci. 74:143–153.

Schaper L, Tankova T, Simões da Silva L, Knobloch M. 2022. A novel residual stress model for welded I-sections. J Constr Steel Res. 188:107017.

Schillo N, Feldmann M. 2017. The rotational capacity of beams made of high-strength steel. Proc Inst Civil Eng Struct Build. 170:641–652.

Schillo N, Feldmann M. 2018. Experiments on the rotational capacity of beams made of high-strength steel. Steel Constr. 11:42–48.

Sedlacek G, Feldmann M. 1995. Background document 5.09 for chapter 5 of eurocode part 1.1 – the b/t ratios controlling the applicability of analysis models in eurocode 3 part 1.1. Report.

Sedlacek G, Feldmann M, Kühn B, Tschickardt D, Höhler S, Müller C, Hensen W, Stranghöner N, Dahl W, Langenberg P, et al. 2008. Commentary and worked examples to en 1993-1-10 "material toughness and through thickness properties" and other toughness oriented rules in en 1993 - background documents in support to the implementation, harmonization and further development of the eurocodes. Report. Europeian Commission Joint Research Centre.

Shi Y, Xu K. 2019. Experimental and analytical study on local buckling behavior of high strength steel welded I-section beams. Int J Steel Struct. 19:1171–1190.

Steenbergen HMGM, Bijlaard FSK, Daniels BJ. 1996. The influence of material properties on plastic hinge rotational capacity and strength. TNO Report 96-CON-R1224. Netherlands Organisation for Applied Scientific Research (TNO).

Stranghöner N, Sedlacek G, Boeraeve P. 1994. Rotation requirement and rotation capacity of rectangular, square and circular hollow section. In: 6. Int. Sympos. on Tubular Struct. Melbourne, Australia.

Timoshenko SP, Gere JM. 1961. Theory of elastic stability. 2nd ed. New York: McGraw-Hill.

Trahair NS, Bradford MA, Nethercot D, Gardner L. 2008. The behaviour and design of steel structures to EC3. 4th ed. Oxon: Taylor & Francis.

Wong WJ, Walters CL. 2021. Failure modes and rules related to the yield-to-tensile strength ratio in steel structures. In: ASME 2021 40th International Conference on Ocean, Offshore and Arctic Engineering (OMAE). ASME (The American Society of Mechanical Engineers). DOI:10.1115/OMAE2021-61995

Yamaki N. 1984. Elastic stability of circular cylindrical shells. Amsterdam: Elsevier Science Publishers BV. (North Holland series in applied mathematics and mechanics).

Yang B, Dong M, Han Q, Elchalakani M, Xiong G. 2021. Flexural behavior and rotation capacity of welded I-beams made from 690-MPa high-strength steel. J Struct Eng. 147:04020320.

Yuan Y, Tan PJ. 2019. On large deformation, damage and failure of ductile plates to blast loading. Int J Impact Eng. 132:Article ID 103330.

Yura JA, Galambos TV, Ravindra MK. 1978. The bending resistance of steel beams. J Struct Div. 104:1355–1370.

Zhu L, Gao J, Li Y. 2018. Numerical analysis on the response of deck plates laterally impacted by a rectangular indenter. In: ASME 2018 37th International Conference on Ocean, Offshore and Arctic Engineering, Madrid, Spain.

Zhu XK, Leis BN. 2005. Influence of yield-to-tensile strength ratio on failure assessment of corroded pipelines. J Press Vessel Technol. 127:436–442.

Appendix. σ_y/σ_u limits found in standards, rules and specifications

Table A1. Limits specified on the nominal values of σ_y/σ_u in design.

Application	σ_y/σ_u limit	Reference
Buildings and bridges	0.95 – elastic analysis 0.91 – plastic analysis	CEN (2020)
Lifting appliances	0.94	LR (2022a) (1)

(1) Additionally, the steel should comply with the LR Rules for the Manufacture, testing and Certification of Materials, in which limits of 0.90 or 0.94 on the actual σ_y/σ_u ratio apply to some steels (see Table A2 below).

(2) In most other design rules or standards, although a limit on σ_y/σ_u is not stated, a requirement is set that the material should comply with relevant product specifications or material certification rules, in which limits on the actual σ_y/σ_u are stated.

Table A2. Limits specified on the actual values of σ_y/σ_u obtained from testing for certification or compliance with product specification.

Application	Steel type	Strength [MPa]	σ_y/σ_u limit	Reference
Buildings, bridges and general structural use	General rolled and HSLA QST steel shapes	345–450	0.85	ASTM (2019, 2020)
Marine and offshore structures	Grades AH, DH, EH, FH	420–960	0.94	LR (2022b) and DNV (2021c)
	C-Mn steels of grades AH, DH, EH, FH–N or M	265–390	0.90	LR (2022b)
	C-Mn steels of grades AH, DH, EH, FH–QT	265–390	0.94	LR (2022b)
	Grades designated with normal weldability, improved weldability 'W' and offshore 'O'	420–960	0.94	DNV (2021b)
	Hot-rolled grades S355–S770: NO, MO, QO	355–770	0.87 (355 MPa)–0.97 (770 MPa)	CEN (2019)
	QR3, QR4, QR4 (offshore mooring chains and accessories)	410–760	0.92	BV (2020)
	High-strength steel for special applications (pressure vessels)	550–690	0.90 (550 MPa)–0.92 or 0.95 (690 MPa)	LR (2022b)
Pipes	Grades L, X with PSL2	245–830	0.93 (245 MPa)–0.99 (830 MPa)	API (2018)
	Grades L, X with PSL2	245–555	0.80 (245 MPa)–0.90 (555 MPa)	ISO (2019)
	C-Mn steels	245–555	0.93	DNV (2021a)
	Duplex and martensitic stainless steels of grades 13Cr, 22Cr, 25Cr	450–550	0.92	DNV (2021a)